

Computer Programs in Physics

DualSPHysics+: An enhanced DualSPHysics with improvements in accuracy, energy conservation and resolution of the continuity equation

Yi Zhan^a, Min Luo^{a,*}, Abbas Khayyer^b^a Ocean College, Zhejiang University, Zhoushan Zhejiang 316021, China^b Department of Civil and Earth Resources Engineering, Kyoto University, Kyoto 615-8540, Japan

ARTICLE INFO

The review of this paper was arranged by Prof Andrew Hazel

Keywords:

Smoothed particle hydrodynamics
Velocity divergence error cleaning
Volume conservation
Riemann-SPH
HPDC
DualSPHysics+

ABSTRACT

This paper presents an enhanced version of the well-known SPH (Smoothed Particle Hydrodynamics) open-source code DualSPHysics for the simulation of free-surface fluid flows, leading to the DualSPHysics+ code. The enhancements are made through incorporation of several schemes with respect to stability, accuracy and energy/volume conservation issues in simulating incompressible free-surface fluid flows within the weakly compressible SPH formalism. The Optimized Particle Shifting (OPS) scheme is implemented to improve the accuracy of particle shifting vectors in the free-surface region. To mitigate energy dissipation and maintain consistency, the artificial viscosity in δ -SPH is substituted with a Riemann stabilization term, leading to the δ R-SPH. The Velocity divergence Error Mitigating (VEM) and Volume Conservation Shifting (VCS) schemes are adopted in DualSPHysics+ to mitigate the velocity divergence error and improve the volume conservation, and hence to enhance the resolution of the continuity equation. To further reduce both the instantaneous and accumulated errors in velocity divergence, a Hyperbolic/Parabolic Divergence Cleaning (HPDC) scheme is incorporated in addition to the VEM scheme. The implementations of the introduced schemes on both CPU and GPU-based versions of the DualSPHysics+ code along with details on the compilation, running and computational performance are presented. Validations in terms of accuracy, energy conservation and convergence of DualSPHysics+ are shown via several relevant benchmarks. It is demonstrated that a better velocity divergence error cleaning in both instantaneous and accumulated errors can be achieved by the combination of VEM and HPDC. Meanwhile, the excessive energy dissipation by the artificial viscosity is shown to be suppressed by adopting the Riemann stabilization term. Enhanced resolution of the continuity equation along with improved energy conservation of DualSPHysics+ advance the SPH-based simulation of incompressible free-surface fluid flows.

Program Summary: Program title: DualSPHysics+.

CPC Library link to program files <https://doi.org/10.17632/xnrfv9pgb5.1>.

Licensing provisions: GNU Lesser General Public License (LGPL).

Programming language: C++, CUDA.

External dependencies: DualSPHysics (<https://dual.sphysics.org>).

Nature of problem: Weakly Compressible Smoothed Particle Hydrodynamics (WCSPH) method and the open-source code DualSPHysics have been widely applied to simulate free-surface fluid flows. Both the general WCSPH method and the more specific DualSPHysics need further improvements in several aspects, including spurious pressure fluctuations, non-conservation of volume and excessive energy dissipation, to enhance the accuracy and stability of simulations.

Solution method: DualSPHysics+ implements a set of numerical schemes to enhance the overall accuracy, divergence-free velocity field, invariant density field and energy conservation in the simulation of free-surface fluid flows based on DualSPHysics.

* Corresponding author.

E-mail address: min.luo@zju.edu.cn (M. Luo).

Descriptions of the key abbreviations used in the paper

Scheme	Abbreviation	Key Equations
Velocity divergence Error Mitigating for suppressing spurious pressure fluctuations in WCSPH	VEM	Eqs. (14), (15)
Volume Conservation Shifting for enhancing the invariant density condition in WCSPH	VCS	Eqs. (19), (20)
Optimized Particle Shifting for consistent implementation of particle shifting at the free-surface region	OPS	Eq. (13)
Hyperbolic/Parabolic Divergence Cleaning for mitigating velocity divergence error	HPDC	Eqs. (33), (34)
Riemann dissipation term for stabilizing simulation while inducing minimal energy dissipation	R	Eqs. (22), (25)

1. Introduction

The Lagrangian particle methods have received extensive interest during the past decade due to their Lagrangian and meshfree nature, as well as their ease of tracking particle motions and handling large deformations of free surfaces [1,2]. Among the various particle methods, the Weakly Compressible Smoothed Particle Hydrodynamics (WCSPH) has been obtaining significant developments and extensive applications in various mechanics and engineering disciplines [3–8]. The open-source DualSPHysics code (<https://dual.sphysics.org>) is fundamentally based on WCSPH for simulation of incompressible free-surface fluid flows. However, some aspects corresponding to the stability, accuracy and energy/volume conservation issues need to be systematically targeted to enhance the reliability of simulations. This paper, through implementation of several enhancing schemes, presents an enhanced version of DualSPHysics, referred to as DualSPHysics+, for more reliable simulations of incompressible free-surface fluid flows within the WCSPH framework.

WCSPH, despite its flexibility and robustness, suffers from the issue of spurious pressure fluctuations or pressure instability incurred by the combined actions of several factors such as the fully-explicit algorithm, collocated spatial discretization, and errors in numerical discretization. One of the causes of pressure fluctuations corresponds to acoustic pressure waves, which are related to the weak compressibility of the fluid flow [9]. In addition, other sources of numerical errors such as the imprecise imposition of boundary conditions or inaccurate estimation of pressure gradient cause inaccuracies in fluid kinematics, which can lead to unphysical noises in velocity divergence and thus further deterioration of density and pressure fields. To resolve the issue, some schemes have been proposed like the artificial viscosity [10], the density filters [11], the density diffusion term [9,12], and the Riemann Solvers [13, 14]. Among them, the δ -SPH introducing conservative diffusive terms for mitigating high-frequency noises [9,15] and the Riemann-SPH evoking the Riemann solver for better modeling of fluid properties at the interface [16,17] have been demonstrated to be effective models and have been widely applied. The artificial viscosity and in general Riemann terms in the momentum equation improve the stability of the system with respect to shocks and discontinuities [18,19] and accordingly enhance the system's kinematics and thus dynamics.

Despite significant advancements in enhancement of stability in the context of WCSPH, one aspect that needs further development is the issue of unphysical density fluctuations in particle scale which leads to unphysical noises in the pressure field. In addition, the lower-frequency acoustic waves with a length scale larger than the radius of the kernel [20] need to be effectively mitigated. For resolving the issues of pressure and density noises, diffusion term-based methods have been proposed. Khayyer et al. [21] developed a velocity divergence error mitigating scheme to enhance the divergence-free velocity field. Sun et al. [20] proposed an acoustic damper term added to the momentum equation to

remove acoustic waves. It is worth noting that these two methods are mathematically equivalent to introducing an extra diffusion term in the momentum equation. Numerical results in the above two studies showed such diffusive-based schemes clearly enhance the pressure fields, especially in problems involving violent impacts. Notwithstanding, some limitations still exist in the diffusion term-based schemes. Firstly, the diffusion term only handles the instantaneous velocity divergence error, but the residual errors in the velocity divergence fields accumulate over time and will contaminate the results in long-term simulations. Secondly, the pressure component derived from the velocity divergence error is obtained through the equation of state; hence an inaccurate estimation of the velocity divergence error, e.g., in case of unphysical kinematics, can result in an inaccurate diffusion term. These limitations prevent the diffusion term-based schemes from being reliably effective in velocity divergence cleaning, i.e., the mitigation of pressure noise, especially in long-term simulations.

A more effective velocity divergence error cleaning method, especially for long-term simulations, is the incorporation of the hyperbolic/parabolic divergence cleaning (HPDC) scheme, which advects and diffuses velocity divergence error by designated hyperbolic and parabolic terms. The HPDC scheme was originally proposed to clean the divergence of magnetic fields in finite volume simulations by Dedner et al. [22] and then successfully applied to smoothed particle magnetohydrodynamics by Tricco et al. [23,24]. Recently, Fourtakas et al. [25] extended the scheme to WCSPH to remove the velocity divergence error without causing excessive dissipation of kinetic energy. However, the accuracy and stability of HPDC in simulating fluid dynamics problems with solid boundaries is yet to be examined.

The second aspect in enhancing the accuracy and reliability of WCSPH simulations corresponds to possible adverse effects caused by the artificial viscosity term commonly used for stabilization of the momentum equation with respect to shocks and discontinuities. This term introduces a dissipative force that is proportional to the velocity difference between neighboring particle pairs [10]. In spite of its effectiveness, the artificial viscosity term can lead to excessive dissipation of the mechanical energy of a fluid system. To partially overcome this issue, ad-hoc conditions for some schemes have been proposed, such as variable artificial viscosity coefficient that is related to velocity divergence [26], switching on or off the dissipation terms based on local flow conditions [27,28], etc. Alternatively, the symmetric kernel gradient correction schemes [29,30] have been proposed to overcome excessive dissipation in numerical models. Although being helpful in improving simulations, these approaches have yet to ensure satisfactory results in terms of energy conservation for general fluid flow simulations.

Another way to achieve numerical stability through introducing proper numerical diffusion is the adoption of a Riemann solver, which estimates fluid properties (e.g., pressure and velocity) at the virtual interface of each particle pair that are close to the real values. The Riemann-based SPH implicitly introduces a certain amount of numerical dissipation to improve numerical stability [31]. However, adopting the linear Riemann solver may also bring in somewhat excessive energy dissipation in the simulations of hydrodynamic problems. Although the issue can be partially addressed by adopting high-order reconstruction schemes for interface properties [32–34] and by using dissipation limiters [16,35], the discretization of the continuity equation in the Riemann solver can adversely affect the global structure of the continuity equation [12], which may further affect the volume conservation of SPH simulations especially when long-term simulations are conducted [36].

To address the research gaps discussed above, this study methodologically considers several enhancing schemes and implements them into the open-source code DualSPHysics, leading to an enhanced version of the code termed DualSPHysics+. The advantageous features of the enhanced code include:

- i) The OPS (Optimized Particle Shifting) scheme [37] is applied to properly implement particle shifting at and in the vicinity of free

- surfaces by effectively eliminating the shifting normal to the free surfaces.
- ii) The second feature corresponds to the combination of the δ -SPH density diffusion term in the continuity equation and a Riemann stabilization term in the momentum equation (instead of the artificial viscosity), abbreviated as δR , to ensure stability, accuracy and minimum energy dissipation without bringing in possible inconsistencies (e.g., violating the global volume conservation due to a non-conserved density diffusion term in the continuity equation). Furthermore, the pressure gradient term in the momentum equation is discretized by the incorporation of a TIC (Tensile Instability Control) [38] to ensure stability and accuracy in tensile stress states.
 - iii) For better numerical resolution of the continuity equation, i.e., ensuring density invariance and velocity divergence free conditions in incompressible free-surface flow simulations, the so-called VCS (Volume Conservation Shifting) [21] and VEM (Velocity divergence Error Mitigating) [21] schemes are newly coded in DualSPHysics+.
 - iv) To further reduce velocity divergence error, especially in long-term simulations, a hyperbolic/parabolic divergence cleaning term [22,23,25] is incorporated in the momentum equation in addition to the VEM scheme. This achieves a more effective cleaning of both instantaneous and accumulated velocity divergence errors. A combination of VEM and HPDC will be effective because VEM tends to clean the instantaneous error in velocity divergence but, at the same time, is prone to inaccurate estimations when unphysical noises exist in fluid kinematics. The HPDC cleans the accumulative errors in velocity divergence through advecting and diffusing them by designed numerical hyperbolic and parabolic terms.

DualSPHysics+, similar to DualSPHysics, is implemented in C++ and CUDA, and enables simulations either on multiple CPUs using OpenMP or on a GPU. The GPU-based version of DualSPHysics+ includes optimized parallelization to maximize speedup, as in case of the original version, i.e., DualSPHysics. DualSPHysics+ enables reliable and efficient simulations of incompressible free-surface fluid flows in both two and three dimensions. The enhancing schemes are implemented in a modular way without affecting the established framework of DualSPHysics. The most enhanced SPH model in DualSPHysics+ is referred to as δR -SPH-OPS-VCS-VEM-HPDC. In brief, δR targets effective stabilization and accuracy enhancement, OPS deals with enhanced particle shifting in free-surface flows, VCS aims at improving invariant density constraint, and VEM/HPDC target the minimization of instantaneous and accumulative errors in the velocity divergence field.

The paper is organized as follows. Section 2 presents the governing equations for SPH simulation of incompressible free-surface fluid flows and Section 3 introduces the formulations of the δ -SPH model with the OPS, VCS and VEM schemes. Section 4 elucidates two further enhancements of the δ -SPH model for better energy conservation and better velocity divergence error cleaning, i.e., δR and HPDC implementations, respectively. Section 5 elaborates the validations of the DualSPHysics+ code based on five benchmark examples including a 3D dam break simulated by the GPU-based version of DualSPHysics+. The program documentation, including the implementation of newly added schemes, sequential algorithm, computational flowchart and the compiling/running details are presented in Section 6 before the concluding remarks of the study in Section 7. The appendix part consists of two appendices. Appendix A comprises three sub-sections presenting information on the computational efficiency of the newly incorporated schemes, the sole performance benefits by OPS and HPDC schemes, and description of a new VEM, referred to as VEM^{II}, suggested to be simultaneously applied with VEM to enhance mitigation of velocity divergence error (especially in the vicinity of free surfaces). Appendix B includes a supplementary document containing all figures with

colourmaps regenerated with a simple light-to-dark blue scheme to ensure there will be no inconvenience for respected readers with Achromatopsia.

2. Governing equations

The fluid flows considered in this study are governed by the conservation equations of mass and momentum, which, in the Lagrangian framework, can be expressed as:

$$\frac{D\rho}{Dt} = -\rho \nabla \cdot \mathbf{u} \quad (1)$$

$$\frac{D\mathbf{u}}{Dt} = -\frac{1}{\rho} \nabla p + \nu \nabla^2 \mathbf{u} + \mathbf{g} \quad (2)$$

where ρ , \mathbf{u} , p and ν stand for fluid density, velocity, pressure and kinematic viscosity, respectively; \mathbf{g} signifies the gravitational acceleration, and t represents time. To model incompressible flows as weakly compressible, an equation of state is utilized to close the conservation equations, as [15,39]:

$$p = c_s^2(\rho - \rho_0) \quad (3)$$

where c_s denotes the speed of sound (the artificial or numerical one is used in WCSPH), and ρ_0 is the reference density of fluid. Note that to portray the effectiveness and reliability of the incorporated schemes, the viscous term in Eq. (2) is not activated. That is, all test cases in this paper consider inviscid fluid flows. However, both laminar [40] and turbulent (including SPS or Sub-Particle-Scale turbulence [40,41]) viscous stresses can be modeled by the DualSPHysics and thus DualSPHysics+.

3. δ -SPH with OPS, VEM and VCS

Particle methods discretize the physical domain into particles that carry physical quantities, including density, velocity, pressure, etc., and discretize the governing equations by particle interpolation schemes [2]. The WCSPH has been extensively applied due to its remarkable performance in both accuracy and efficiency. However, the traditional WCSPH suffers from the issue of spurious pressure fluctuations. To address this issue, the density diffusion term has been proposed [9], the improved version of which is the so-called δ -SPH [9,15]. The particle-interpolation form of the governing equations of δ -SPH reads:

$$\frac{D\rho_a}{Dt} = -\rho_a \sum_b \mathbf{u}_{ab} \cdot \nabla_a W_{ab} V_b + D_a \quad (4)$$

$$\frac{D\mathbf{u}_a}{Dt} = -\sum_b m_b \left(\frac{p_b + p_a}{\rho_b \rho_a} + \Pi_{ab} \right) \nabla_a W_{ab} + \mathbf{g} \quad (5)$$

$$\frac{Dr_a}{Dt} = \mathbf{u}_a, \quad (6)$$

$$p_a = c_s^2(\rho_a - \rho_0), \quad (7)$$

where a denotes the target particle and b indicates the neighbor particles within the supporting radius; $\mathbf{u}_{ab} = \mathbf{u}_a - \mathbf{u}_b$; W is the kernel function and the fifth-order C2 Wendland kernel [42] is adopted in this paper. The smoothing length $h = 2.0 dp$ is used with dp being the initial particle spacing. The artificial speed of sound $c_s = 10U_{\max}$ is selected (U_{\max} is the maximum particle velocity in the simulation) to allow feasible time step size and guarantee the weak compressibility of fluid [11]. The particle interpolated density diffusion term D and the associated terms read [43]:

$$D_a = \delta h c_s \sum_b \psi_{ab} \cdot \nabla_a W_{ab} V_b \quad (8)$$

$$\psi_{ab} = 2(\rho_{ba}^T - \rho_{ab}^H) \frac{\mathbf{r}_{ab}}{|\mathbf{r}_{ab}|^2} \quad (9)$$

$$\rho_{ba}^T = \rho_b - \rho_a; \rho_{ab}^H = p_{ab}^H/c_s^2; p_{ab}^H = \rho_0 \mathbf{g} \cdot \mathbf{r}_{ab} \quad (10)$$

where the superscripts $(\cdot)^T$ and $(\cdot)^H$ denote the total and hydrostatic components of density. p_{ab}^H denotes the hydrostatic pressure difference between particles a and b . The parameter δ is taken as 0.1 [15].

The artificial viscosity term, Π , which was proposed to prevent unphysical particle penetrations and to stabilize simulations [10], reads:

$$\Pi_{ab} = \begin{cases} \left(\frac{-\alpha c_{ab}}{\bar{\rho}_{ab}} \right) \left(\frac{h \mathbf{u}_{ab} \cdot \mathbf{r}_{ab}}{|\mathbf{r}_{ab}|^2 + \eta^2} \right) & \mathbf{u}_{ab} \cdot \mathbf{r}_{ab} < 0 \\ 0 & \mathbf{u}_{ab} \cdot \mathbf{r}_{ab} \geq 0 \end{cases} \quad (11)$$

where α is a tunable coefficient, $\mathbf{r}_{ab} = \mathbf{r}_a - \mathbf{r}_b$; $\bar{\rho}_{ab} = \frac{\rho_a + \rho_b}{2}$; $c_{ab} = c_s$ for single-phase simulations; $\eta^2 = 0.01h^2$ is adopted to guarantee a non-singular operator. Regarding other numerical schemes, the predictor-corrector scheme [44] with the time step size determined by the Courant–Friedrich–Levy (CFL) condition [45] is adopted for time integration. The dummy particle technique [46] is used to model the solid boundaries, in which the solid boundaries are discretized into several layers of dummy particles with physical quantities extrapolated from the fluid particles. The non-slip boundary condition is applied.

3.1. Optimized particle shifting (OPS)

The δ -SPH has been enhanced by the particle shifting technology [7, 31, 47, 48], which leads to a more uniform particle distribution and hence better accuracy and stability. After a fluid particle is advected in each time step, its position is slightly shifted as:

$$\dot{\mathbf{r}}_a = \mathbf{r}_a + \delta \mathbf{r}_a^{\text{OPS}} \quad (12)$$

where \mathbf{r}_a , $\delta \mathbf{r}_a^{\text{OPS}}$ and $\dot{\mathbf{r}}_a$ signify the particle position after solving the momentum equations, the shifting vector, and the particle position after shifting, respectively. A well-known particle shifting scheme was developed based on the Fick's law of diffusion [49–51]. To enhance the applicability of the shifting scheme in the free-surface region, Khayyer et al. [37] have proposed the optimized particle shifting (OPS) scheme by eliminating the normal shifting component for free-surface and free-surface-vicinity particles. In this scheme, the shifting vector for the free-surface and free-surface-vicinity particles reads [37]:

$$\delta \mathbf{r}_a^{\text{OPS}} = -C_{\text{shift}} h^2 \nabla_S C_a = -C_{\text{shift}} h^2 (\nabla C_a - \nabla_N C_a) = -C_{\text{shift}} h^2 \left(\mathbf{I} - \tilde{\mathbf{n}}_a \otimes \tilde{\mathbf{n}}_a \right) \cdot \nabla C_a \quad (13)$$

where C stands for the particle concentration; the subscript $(\cdot)_S$ and $(\cdot)_N$ denote the tangential and normal components, respectively; C_{shift} is a constant number taken to be < 0.5 ; $\tilde{\mathbf{n}}_a$ is a unit normal vector for free-surface particle [37, 52]; \mathbf{I} is an identity matrix. The maximum value of $|\delta \mathbf{r}_a^{\text{OPS}}|$ is set to be $h/20$ based on parametric studies [21], which is small compared to the advective displacement. The free-surface and free-surface-vicinity particles are detected based on the position vector divergence criterion and more details of the detection criteria are referred to Khayyer et al. [21, 37].

Note that in addition to OPS, Michel et al. [53] proposed a consistent shifting velocity by using a relative velocity between particles instead of the absolute velocity. Lyu et al. [48] proposed a corrective shifting vector to address the issue of fluid volume non-conservation. Rastelli et al. [54] incorporated the Implicit Iterative Particle Shifting (IIPS)

formulation in an SPH-ALE solver with careful update of physical quantities at the end of the implicit procedure to ensure consistency. These shifting schemes can also be considered in the framework of DualSPHysics+.

3.2. Velocity divergence error mitigating (VEM)

In the simulation of incompressible flows, it is essential to reproduce a spatially continuous zero velocity divergence field. In δ -SPH (and other WCPH variants), the divergence of velocity is not enforced to be zero and is not necessarily spatially continuous due to the weakly compressible assumption and discretization errors. These lead to unphysical fluid quantities like spurious density and pressure fluctuations [20, 21]. The density diffusion term in δ -SPH tends to filter the spurious fluctuations at a length scale comparable to the kernel radius [20]. However, such fluctuations cannot be fully removed especially those in a scale larger than the kernel radius, such as the acoustic waves reported in some studies [20, 21, 55]. In addition, as a discretized numerical term, the density diffusion term will have a certain order of accuracy. Khayyer et al. [21] have proposed the VEM scheme to compensate for the deviation of instantaneous velocity divergence from zero, which enhances the spatial continuity and physical consistency of the velocity divergence field.

In VEM, an additional pressure term p_a^{VEM} at the current time step k is computed based on the deviation of the velocity divergence field from zero at time step $k-1$, as:

$$p_a^{\text{VEM}} = c_s^2 d\rho_a = c_s^2 \Delta t \left(\frac{D\rho}{Dt} \right)_a^{k-1} = -\rho_a c_s^2 \Delta t \langle \nabla \cdot \mathbf{u} \rangle_a^{k-1} \quad (14)$$

The pressure component corresponds to an acceleration component $\mathbf{a}_a^{\text{VEM}}$ as:

$$\mathbf{a}_a^{\text{VEM}} = -\frac{1}{\rho_a} \sum_b F(p_a^{\text{VEM}}, p_b^{\text{VEM}}) \nabla_a W_{ab} V_b \quad (15)$$

$$F(p_a, p_b) = \begin{cases} p_b + p_a & (p_a \geq 0 \cup a \notin \Omega_{IN}) \\ p_b - p_a & (p_a < 0 \cap a \in \Omega_{IN}) \end{cases} \quad (16)$$

where F is an operator incorporating the Tensile Instability Control (TIC) technique [38] that is beneficial for cases with strong negative pressures; Ω_{IN} denotes the inner fluid region. The fluid particle acceleration is then added into the momentum equation as an additional error-mitigating term as:

$$\frac{D\mathbf{u}_a}{Dt} = -\sum_b m_b \left(\frac{F(p_a, p_b)}{\rho_a \rho_b} + \Pi_{ab} \right) \nabla_a W_{ab} + \mathbf{g}_a + \mathbf{a}_a^{\text{VEM}} \quad (17)$$

3.3. Volume conservation shifting (VCS)

In particle-based simulations of incompressible fluid flows, it is also important to maintain the invariant density condition. That is, the kernel summation density should be equal to the reference density, expressed as:

$$\tilde{\rho}_a = \tilde{\rho}_0; \tilde{\rho}_a = \sum_b m_b W_{ab} \quad (18)$$

where $\tilde{\rho}_a$ denotes the density based on the kernel summation and $\tilde{\rho}_0$ corresponds to its reference value at the initial stage. Discrete density defined by Eq. (18) is of vital importance to ensure that the continuum density will be recovered through refinement of particle spacing. The δ -SPH and many other SPH variants do not impose the constant density condition, which implies that the volume conservation, especially in long-term simulations, cannot be guaranteed. In addition, the use of the particle shifting technology will induce unphysical volume changes [7, 31, 48]. Pilloton et al. [56] have recently presented some techniques for measuring volume conservation errors and proposed two stabilization terms in an attempt to improve volume conservation in Weakly Compressible SPH simulations. Inspired by the projection-based particle method, Khayyer et al. [21] have proposed the VCS scheme, which compensates for numerical errors related to the deviation of particle density with respect to the reference density. A pressure term corresponding to the VCS scheme, i.e., p^{VCS} , is computed by explicitly solving a PPE (Poisson Pressure Equation) with the volume conservation error as the source term, as:

$$\left\{ \nabla \cdot \left(\frac{\nabla p^{\text{VCS}}}{\rho} \right) \right\}_a^{k+1} = \frac{\tilde{\rho}_0 - \tilde{\rho}_a^k}{\tilde{\rho}_0 \Delta t^2} + \frac{1}{\Delta t^2 \tilde{\rho}_0 c_s^2} p_a^{\text{VCS}, k+1} \quad (19)$$

where Δt is the time step. Note that the PPE involving VCS pressure is solved explicitly, and hence, this step can be computed efficiently (costing <10% of the total computational time) [1]. The Dirichlet boundary condition $p^{\text{VCS}} = 0$ is imposed to the free-surface particles. Regarding the free-surface-vicinity particles, the interpolation from the nearest inner fluid particles is conducted. On solid wall boundaries, the Neumann boundary condition $\frac{\partial p^{\text{VCS}}}{\partial n} = 0$ is imposed. Note that p^{VCS} leads to additional particle acceleration and, hence, to another particle shifting vector δr_a^{VCS} , as follows:

$$\delta r_a^{\text{VCS}} = \Delta t^2 \left(-\frac{1}{\rho_a} \langle \nabla p^{\text{VCS}} \rangle_a^L \right) \quad (20)$$

where the superscript $(\cdot)^L$ denotes the renormalized gradient [21]. The maximum value of $|\delta r_a^{\text{VCS}}|$ is set to be $h/20$ and the VCS shifting vector is integrated into the particle position shifting at each calculation time step, i.e., Eq. (12), as:

$$\dot{r}_a = r_a + \delta r_a^{\text{OPS}} + \delta r_a^{\text{VCS}} \quad (21)$$

The VEM scheme yields notable improvement in achieving the divergence-free velocity, and the VCS scheme effectively enhances the invariant density condition. The two schemes together lead to a more accurate, physically consistent, and numerically resolved representation of the continuity equation in WCSPH simulations, particularly for incompressible free-surface fluid flows [21]. However, some aspects still need further improvements, such as the excessive mechanical energy dissipation due to the artificial viscosity and the accumulated velocity divergence error, especially in long-term simulations.

4. Further enhancements of δ -SPH

4.1. δ R-SPH for enhancement of energy conservation

Compared to the δ -SPH presented in Section 3, the Riemann-based SPH model introduces the numerical dissipation term (needed for stability) more physically than the artificial viscosity [57]. Hence, one approach to address the issue of excessive energy dissipation is to adopt the Riemann solver [17, 33, 57, 58]. However, as highlighted by Khayyer et al. [36], the discretization of the continuity equation in Riemann SPH can lead to the non-conservation of the diffused numerical density on the global scale, which adversely affects the volume conservation of the numerical model. Therefore, a combination of the δ -SPH and the Riemann-based SPH is adopted, leading to the δ R-SPH. In δ R-SPH, the discretized continuity equation is the same as Eq. (4). The discretized

momentum equation is as follows:

$$\frac{D\mathbf{u}_a}{Dt} = -2 \sum_b m_b \left(\frac{p^*}{\rho_a \rho_b} \right) \nabla_a W_{ab} + \mathbf{g} \quad (22)$$

$$p^* = \frac{1}{2} F(p_L, p_R) + \frac{1}{2} \bar{\rho} c_s (u_L - u_R) \quad (23)$$

where $\bar{\rho} = \frac{2\rho_L \rho_R}{\rho_L + \rho_R}$ and $F(p_L, p_R)$ is defined in the same manner as Eq. (16) and implies the adoption of the TIC scheme. The fluid quantities at the left state L and the right state R are determined by those at particles a and b , as follows:

$$\begin{cases} (\rho_L, u_L, p_L) = (\rho_a, \mathbf{u}_a \cdot \mathbf{e}_{ab}, p_a) \\ (\rho_R, u_R, p_R) = (\rho_b, \mathbf{u}_b \cdot \mathbf{e}_{ab}, p_b) \end{cases} \quad (24)$$

where the unit vector $\mathbf{e}_{ab} = -\mathbf{r}_{ab}/|\mathbf{r}_{ab}|$ points from particle a to b . To overcome the excessive numerical dissipation associated with Eq. (23), Zhang et al. [16] proposed a dissipation limiter to the intermediate pressure such that the dissipation is applied when the fluid undergoes compression. Also inspired by Xue et al. [35], the improved dissipation limiter concerning the distance between a pair of particles is adopted, as:

$$p^* = \frac{1}{2} F(p_L, p_R) + \frac{1}{2} \phi \bar{\rho} (u_L - u_R) \quad (25)$$

$$\phi = \frac{\beta \bar{h}_{ab}}{|\mathbf{r}_{ab}|} \min \{ \max[(u_L - u_R), 0], c_s \} \quad (26)$$

where $\bar{h}_{ab} = \frac{h_a + h_b}{2}$ is the averaged smoothing length of particles a and b . In Eq. (26), β is a coefficient recommended to be smaller than 30 based on parametric tests [35], and $\beta = 15$ is adopted in the present study unless otherwise stated. The dimensionless coefficient $\frac{\bar{h}_{ab}}{|\mathbf{r}_{ab}|}$ indicates that the amount of numerical dissipation is proportional to the distance between a particle pair. The interaction between a fluid particle and a dummy wall particle can be considered as a one-sided Riemann problem [16].

It is noteworthy that the δ R-SPH model, due to the combination of the advantages of the δ diffusive and Riemann stabilization terms, mitigates the issue of excessive energy dissipation partially induced by the artificial viscosity and circumvents the inconsistency introduced by the conventional Riemann solver discretization of the continuity equation [36]. It should also be highlighted that the δ term has a close similarity to the Riemann terms incorporated in the continuity equation as also discussed by Khayyer et al. [59]. In other words, the δ R-SPH model can be considered as a specific Riemann SPH model. However, we prefer to use the abbreviation of δ R-SPH because the diffusive term in the continuity equation has already been incorporated in the context of δ -SPH models [15, 43] and in contrast to some commonly applied Riemann SPH terms in the continuity equation (e.g., [16, 60, 61]), the δ term perfectly ensures global volume conservation.

4.2. HPDC for further enhanced velocity divergence error cleaning

Regarding the issue of velocity divergence error in δ -SPH, although the VEM scheme reduces numerical errors in each computational step, limitations still exist. Firstly, with possibly unphysical kinematics such as noises in the velocity field, the VEM scheme that relies on fluid velocity data may lead to unphysical accelerations, which further contaminate the simulated velocity and density fields. Secondly, the pressure p_a^{VEM} is only related to the instantaneous velocity divergence error, i.e., the undesired density deviation induced during one typical calculation time step, which means the error cleaning is effective only for the instantaneous velocity divergence field and numerical errors accumulate in time.

To partially overcome the first issue, a threshold for the magnitude of

δ -SPH model in DualSPHysics

$$\begin{aligned}\frac{D\rho_a}{Dt} &= -\rho_a \sum_b \mathbf{u}_{ab} \cdot \nabla_a W_{ab} V_b + D_a \\ \frac{D\mathbf{u}_a}{Dt} &= -\sum_b m_b \left(\frac{p_b + p_a}{\rho_b \rho_a} + \Pi_{ab} \right) \nabla_a W_{ab} + \mathbf{g}\end{aligned}$$

Further enhancements corresponding to four aspects

- i) Minimum energy dissipation \leftarrow Riemann stabilization term (Eqs. 22, 25) instead of artificial viscosity
- ii) Consistent particle shifting at and in the vicinity of free surface \leftarrow OPS (Eq. 13)
- iii) Enhanced resolution of the continuity equation \leftarrow VEM and VCS (Eqs. 14-20)
- iv) Effective cleaning of velocity-divergence errors \leftarrow Combination of VEM and HPDC (Eqs. 32-34)

δ R-SPH-OPS-VCS-VEM-HPDC in DualSPHysics+

$$\begin{aligned}\frac{D\rho_a}{Dt} &= -\rho_a \sum_b \mathbf{u}_{ab} \cdot \nabla_a W_{ab} V_b + D_a \\ \frac{D\mathbf{u}_a}{Dt} &= -2 \sum_b m_b \left(\frac{\mathbf{p}^*}{\rho_a \rho_b} \right) \nabla_a W_{ab} + \mathbf{g} + \mathbf{a}_a^{\text{VEM}} - \nabla \psi_a, \quad p^* = \frac{1}{2} F(p_L, p_R) + \frac{1}{2} \phi \bar{\rho} (u_L - u_R) \\ \mathbf{r}'_a &= \mathbf{r}_a + \delta \mathbf{r}_a^{\text{OPS}} + \delta \mathbf{r}_a^{\text{VCS}}\end{aligned}$$

Fig. 1. Further enhancements in four aspects and the key formulations of the developed DualSPHysics+.

the VEM approximated acceleration is introduced to avoid excessive modification of the fluid kinematics. In the present study, the threshold value is selected to be $|\mathbf{a}_a|/10$ based on parametric studies, where $|\mathbf{a}_a|$ is the acceleration corresponding to the pressure gradient term for particle a . Regarding the second issue mentioned above, i.e., the accumulated velocity divergence error, a hyperbolic/parabolic divergence cleaning (HPDC) scheme is adopted, which has been proposed for cleaning the divergence of magnetic fields [22–24] and has been extended by Fourtakas et al. [25] for mitigating the acoustic waves in WCSPH. In HPDC, the divergence-free constraint for the velocity field is coupled with the evolution of velocity (i.e., the momentum equation) by introducing a new scalar field ψ as [22]:

$$\left(\frac{D\mathbf{u}}{Dt} \right)_\psi + \nabla \psi = 0 \quad (27)$$

$$\mathcal{D}(\psi) + \nabla \cdot \mathbf{u} = 0 \quad (28)$$

where \mathcal{D} is a linear differential operator that can be an elliptic correction, a hyperbolic correction, etc. For numerical stability and efficiency, the mixed hyperbolic and parabolic correction term has been suggested, as:

$$\mathcal{D}(\psi) = \frac{1}{c_h^2} \frac{D\psi}{Dt} + \frac{1}{c_p^2} \psi \quad (29)$$

where c_h is the fastest wave speed; c_p is a diffusion parameter that can be evaluated by relating c_h and the smoothing length h as $\sqrt{2hc_h/\pi}$ [25]. By substituting $\mathcal{D}(\psi)$ into Eq. (28), the evolution of field ψ can be expressed as:

$$\frac{D\psi}{Dt} = -c_h^2 (\nabla \cdot \mathbf{u}) - \frac{c_h^2}{c_p^2} \psi \quad (30)$$

The first term on the right-hand side of Eq. (30) is a hyperbolic term advecting the local velocity divergence error away from the source by the fastest wave speed c_h . The second term is a parabolic term diffusing velocity divergence error locally. Note that once velocity divergence error accumulate, ψ becomes nonzero and the hyperbolic/parabolic

terms are activated.

Taking the gradient of Eq. (30) and substituting it into Eq. (27) and then taking the divergence of velocity, the damped wave equation for the divergence of velocity field can be obtained as:

$$\frac{\partial^2 (\nabla \cdot \mathbf{u})}{\partial t} - c_h^2 \nabla^2 (\nabla \cdot \mathbf{u}) + \frac{c_h^2}{c_p^2} \frac{\partial (\nabla \cdot \mathbf{u})}{\partial t} = 0 \quad (31)$$

Eq. (31) indicates that the unphysical errors or noises in the velocity divergence field can be eliminated by advection through the hyperbolic term and diffusion through the parabolic term.

It should be noted that in the recent paper by Fourtakas et al. [25], the HPDC scheme was compared against a diffusive divergence cleaning scheme referred to as acoustic damper [20] (which is similar to the VEM scheme). Combined application of diffusive and hyperbolic/parabolic divergence cleaning has not been considered in the paper by Fourtakas et al. [25]. For the conducted test cases in [25] corresponding to a divergence blob test [24] and impact of two rectangular fluid patches [55], both diffusive and hyperbolic/parabolic divergence cleaning schemes were shown to be effective to some extend in reducing the velocity divergence error in the domain. Specifically, for the divergence blob test, the effectiveness of HPDC was shown to be superior compared to the acoustic damper term. Based on the fluid patches impact test, Fourtakas et al. [25] showed that the HPDC scheme is less diffusive than the acoustic damper.

The VEM scheme is effective in mitigating the instantaneous velocity divergence error as it is based on deviations in instantaneous velocity divergence field. On the other hand, the HPDC scheme targets the existing accumulated and instantaneous errors in the velocity divergence field to be cleaned by advective and diffusive terms in Eq. (31). Thus, simultaneous activation of the VEM and HPDC schemes is expected to result in effective cleaning of the velocity divergence error in the physical domain. For inheriting the above advantages, the δ R-SPH model elaborated in Section 4.1 is further improved by incorporating the VEM and HPDC schemes for enhanced cleaning of the instantaneous and accumulated (essential in long-term simulations) velocity divergence error, which leads to the δ R-SPH-OPS-VCS-VEM-HPDC model.

In the particle interpolation framework, the momentum equation of

Table 1

Pseudocode of the δ R-SPH-OPS-VCS-VEM-HPDC model in DualSphysics+.

Algorithm 1: Key computations in a time step in δ R-SPH-OPS-VCS-VEM-HPDC model

```

1:   while Time < TimeMax do
2:     //—— Predictor Step——
3:     Conduct Cell-link list
4:     Compute the renormalization matrix and the normal vectors, and conduct
5:       particle categorization
6:       for  $a \in$  fluid particles, do
7:         Compute  $p_a^{\text{VEM}}$  (Eq. (14)) and  $p_a^{\text{VCS}}$  (Eq. (19))
8:       end for
9:       for  $a \in$  fluid particles, do
10:        Compute  $a_a^{\text{VEM}}$  (Eq. (15)),  $\delta r_a^{\text{VCS}}$  (Eq. (20)) and  $\delta r_a^{\text{OPS}}$  (Eq. (13))
11:      end for
12:      Impose boundary conditions for  $\rho$ ,  $p$ ,  $u$ ,  $\psi$ 
13:      for  $a \in$  fluid particles, do
14:        Compute  $D\rho_a/Dt$ ,  $Du_a/Dt$ ,  $D\psi_a/Dt$ , etc. for particle interactions
15:      end for
16:      Time integration from  $t = k$  to  $k + 1/2$ 
17:      //—— Corrector Step——
18:      Conduct Cell-link list
19:      Impose boundary conditions for  $\rho$ ,  $p$ ,  $u$ ,  $\psi$ 
20:      for  $a \in$  fluid particles, do
21:        Compute  $D\rho_a/Dt$ ,  $Du_a/Dt$ ,  $D\psi_a/Dt$ , etc. for particle interactions
22:      end for
23:      for  $a \in$  fluid particles, do
24:        Add  $a_a^{\text{VEM}}$  into  $Du_a/Dt$  for each fluid particle
25:        Apply shifting vector:  $\delta r_a^{\text{OPS}}$ ,  $\delta r_a^{\text{VCS}}$  by Eq. (21)
26:      end for
27:      Time integration from  $t = k + 1/2$  to  $k + 1$ .
28:      Update time step size  $\Delta t$  for the next computational step
29:    end while

```

the δ R-SPH-OPS-VCS-VEM-HPDC model can be written as:

$$\frac{Du_a}{Dt} = -2 \sum_b m_b \left(\frac{p^*}{\rho_a \rho_b} \right) \nabla_a W_{ab} + \mathbf{g} + \mathbf{a}_a^{\text{VEM}} - \nabla \psi_a \quad (32)$$

Note that the OPS and VCS terms are considered in the particle shifting step, i.e., Eq. (21). The ψ gradient term can be discretized as [25]:

$$\nabla \psi_a = - \sum_b \frac{m_b}{\rho_b} \psi_{ab} \nabla_a W_{ab} \quad (33)$$

where $\psi_{ab} = \psi_a - \psi_b$. The time derivative of ψ , i.e., Eq. (30), can be discretized as:

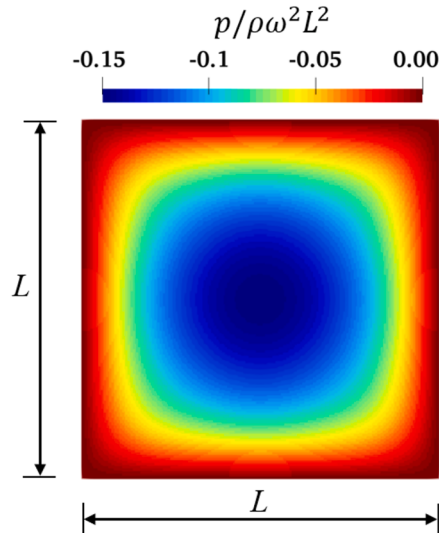


Fig. 2. Initial distributions of pressure and velocity in the rotating square patch.

$$\frac{D\psi_a}{Dt} = c_h^2 \sum_b \frac{m_b}{\rho_b} \mathbf{u}_{ab} \cdot \nabla_a W_{ab} - \frac{c_h^2}{c_p^2} \psi_a \quad (34)$$

The initial value of ψ can be set to 0 and updated at each time step according to Eq. (34). From the physical point of view, ψ ought to vanish and the velocity divergence error should not accumulate at solid boundaries. Hence, the Dirichlet boundary condition $\psi = 0$ is imposed at solid boundaries.

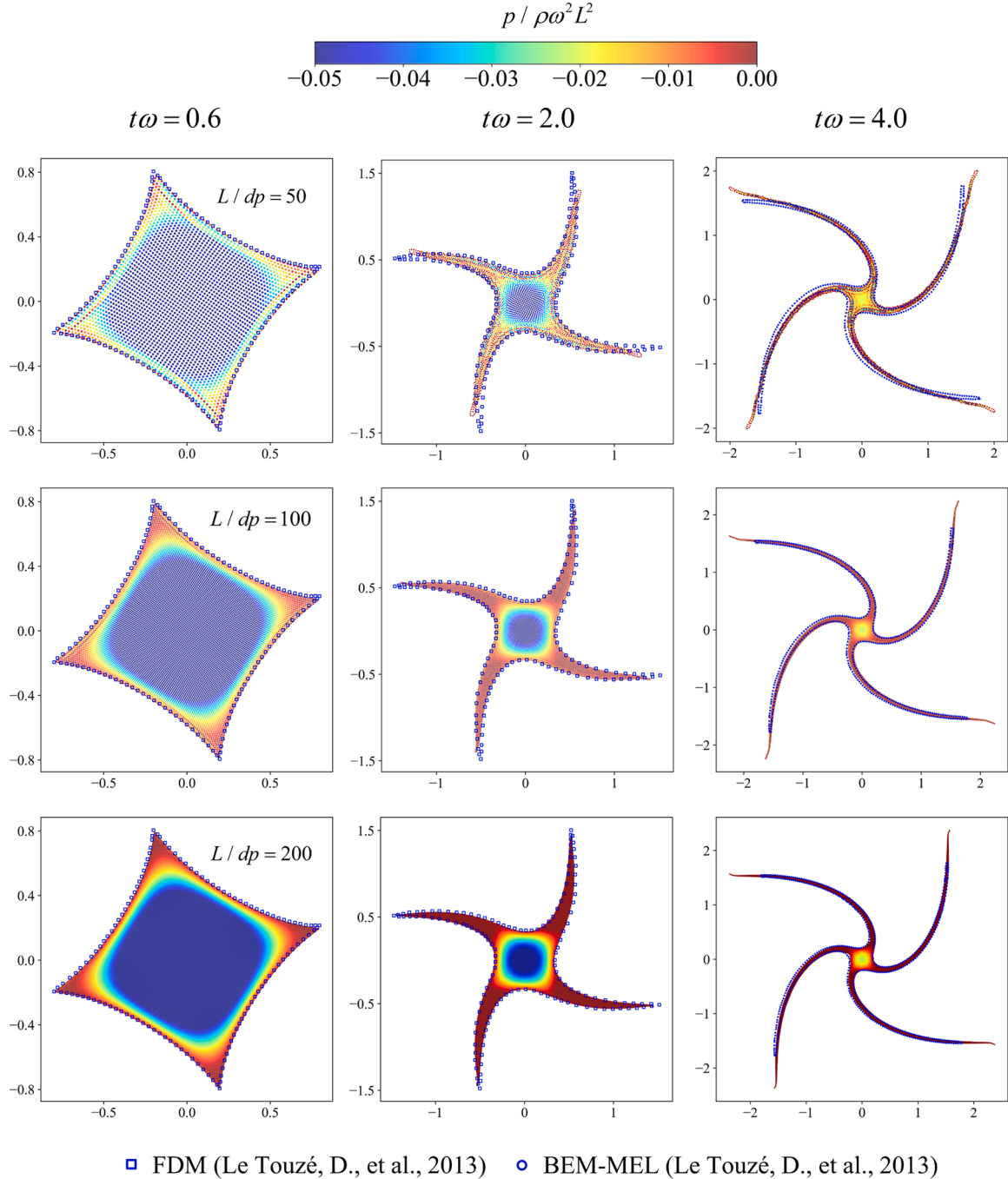
In summary, this study proposes the simultaneous application of VEM and HPDC schemes for effective minimization of the instantaneous and accumulated velocity divergence error. The VEM tends to minimize only the instantaneous velocity divergence error while the HPDC mainly targets the accumulated velocity divergence error, i.e., the error that has not been mitigated by the VEM scheme. It should be noted that accelerations corresponding to VEM and HPDC schemes are approximations and thus, one should not expect “perfect” velocity divergence cleaning even by simultaneous applications of these two schemes. However, this paper shows that the simultaneous application of VEM and HPDC effectively and clearly minimizes the errors in velocity divergence field.

4.3. Sum-up notes of DualSphysics+

As a sum-up note of Section 4, Fig. 1 presents the summary of the enhancements in four aspects for DualSPhysics, including the minimum energy dissipation, consistent particle shifting at and in the vicinity of free surfaces, enhanced resolution of the continuity equation, and effective cleaning of velocity divergence error, leading to DualSPhysics+. The pseudocode of the developed δ R-SPH-OPS-VCS-VEM-HPDC model in DualSphysics+ is presented in Table 1.

5. Numerical investigations

Five benchmark test cases are conducted to test the performance of the DualSPhysics+, including the enhancing schemes δ R-SPH, OPS, VCS, VEM and HPDC. The considered five benchmark tests are a rotating fluid square [62], the impact of two rectangular fluid patches [63], a two-dimensional dam break [64], liquid sloshing under roll excitations [65] and a three-dimensional dam break [66]. The last test case presented in Section 5.5 includes simulations by the GPU-based version of DualSPhysics+, illustrating the enhancing performance of the new schemes in 3D and on GPU.



□ FDM (Le Touzé, D., et al., 2013) ○ BEM-MEL (Le Touzé, D., et al., 2013)

Fig. 3. Fluid particle distributions with pressure contours at $t\omega = 0.6, 2.0$ and 4.0 by δ R-SPH-OPS-VCS-VEM-HPDC. The particle resolutions from the top to bottom rows are $L/dp = 50, 100, 200$, respectively - a rotating fluid square.

5.1. A rotating fluid square

Firstly, the rotation of a square fluid patch with initial negative pressure [37,47,48,67] is simulated to validate the proposed schemes, especially in handling negative pressure and large free-surface deformations. In this case, an inviscid fluid patch of the square shape with a side length L deforms under an initially rotating velocity field defined as (see Fig. 2):

$$\mathbf{u}(x, y, 0) = (\omega y; -\omega x) \quad (35)$$

where ω is a constant describing the rotating rate. In this study, $L = 1$ m, $\omega = 1$ rad s⁻¹ and the sound speed $c_s = 15$ m s⁻¹ are adopted; the initial density of the fluid is 1000 kg/m³; The initial pressure of the problem is

governed by a Poisson equation, which can be evaluated by solving a series expansion equation [68].

The particle resolution convergence of the proposed δ R-SPH-OPS-VCS-VEM-HPDC model is firstly examined by testing three different particle resolutions, i.e., $L/dp = 50, 100$ and 200 , which correspond to the coarse, middle and fine resolutions, respectively. As shown in Fig. 3, at the early stage of the fluid patch rotating (e.g., at $t\omega = 0.6$), the morphologies predicted by the three particle resolutions all match well with the documented FDM (Finite Difference Method) result [62], while the pressure distributions produced by the coarse resolution show slight noises especially in the tip regions. As the fluid patch further deforms (e.g., until $t\omega = 2.0$ and 4.0), the unphysical tip shapes and pressure noises become more evident in the coarse resolution simulation. In contrast,

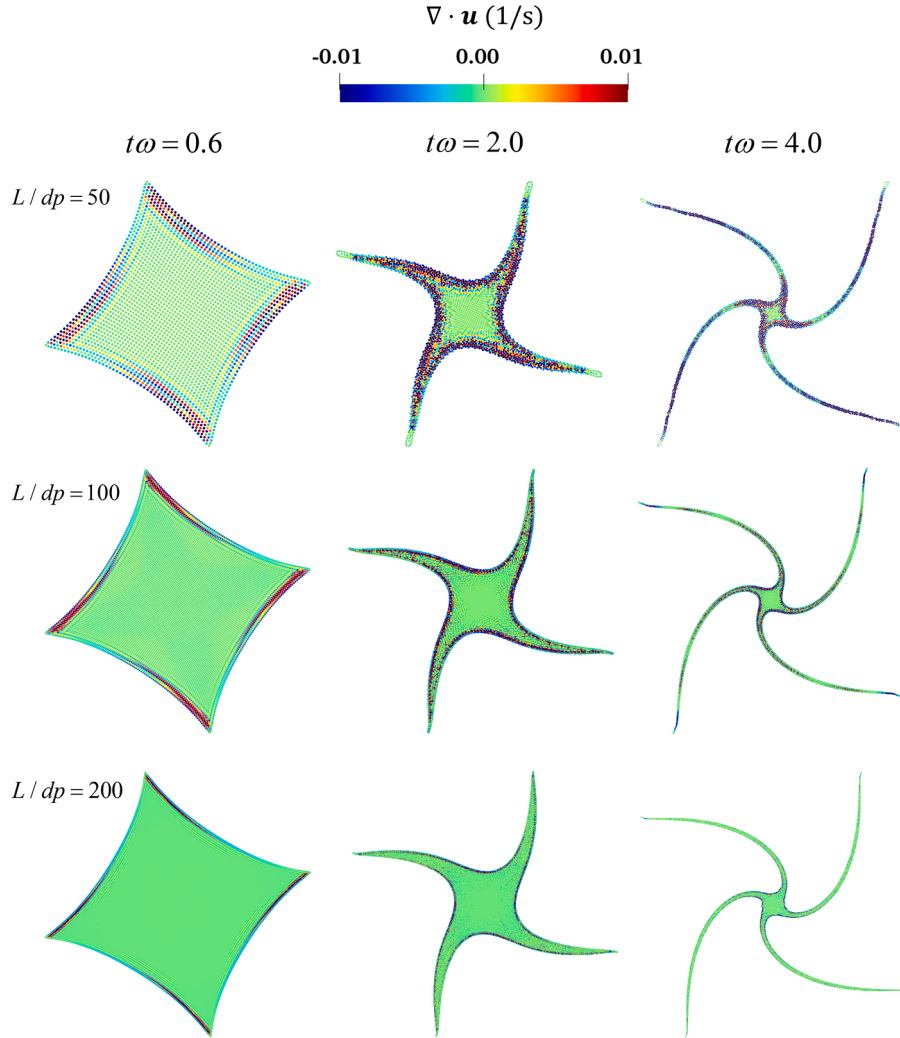


Fig. 4. Fluid particle distributions with velocity divergence contours at $t\omega = 0.6, 2.0$ and 4.0 by δR -SPH-OPS-VCS-VEM-HPDC. The particle resolutions from the top to bottom rows are $L/dp = 50, 100, 200$, respectively - a rotating fluid square.

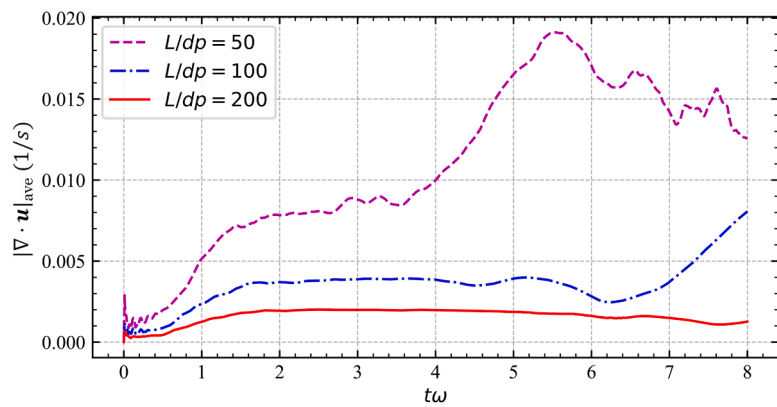


Fig. 5. Time histories of the average absolute value of the velocity divergence error by δR -SPH-OPS-VCS-VEM-HPDC with three different resolutions - a rotating fluid square.

the middle and fine resolutions can better capture the large spatial variation of fluid quantities. Their results of the highly-deformed tip shapes are quite close and agree well with the reference benchmark results, and the pressure contours are physically smooth and the negative pressures are successfully reproduced. These results qualitatively demonstrate the convergence and accuracy in simulating large

deformations of free surfaces and negative pressures.

The velocity divergence fields by three different particle resolutions are shown in Fig. 4. In the results of the coarse resolution, evident velocity divergence error can be observed, in particular, near the free-surface boundaries and the tip regions. With the refinement of particle resolution, the errors are significantly reduced and more continuous

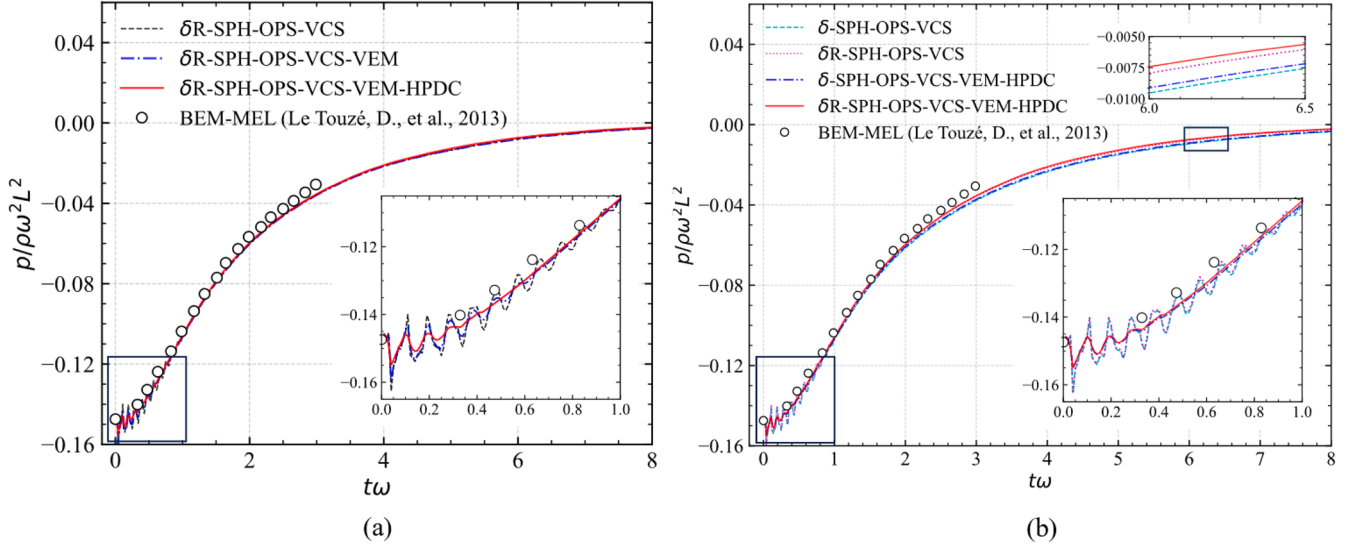


Fig. 6. Pressure histories at the center of the square patch simulated by δ R-SPH-OPS-VCS, δ R-SPH-OPS-VCS-VEM and δ R-SPH-OPS-VCS-VEM-HPDC, in the particle resolution of $L/dp = 100$ - a rotating fluid square.

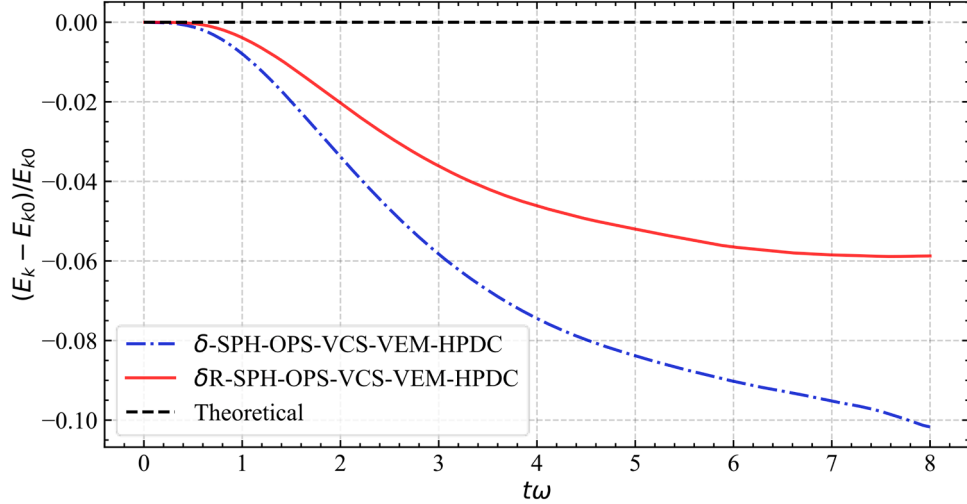


Fig. 7. Time histories of normalized kinetic energy calculated by δ -SPH-OPS-VEM-HPDC, and δ R-SPH-OPS-VEM-HPDC, in the particle resolution of $L/dp = 100$ - a rotating fluid square.

velocity divergence fields are obtained. Fig. 5 shows the average absolute value of the velocity divergence error $|\nabla \cdot \mathbf{u}|_{\text{ave}}$ at discrete calculation points (particles) in the domain, which is evaluated as $\sum_i^N |\nabla \cdot \mathbf{u}_i| / N$ (N stands for the total number of particles in the domain). This term is an indicator of the volume time rate error in particle scale in each conducted simulation. The average error drops significantly with the refinement of particle resolution and approaches zero in the finest resolution studied here. Also, the time history of the average velocity divergence error in the finest resolution is more stable in the whole simulation process as compared to those of the coarser resolution simulations. The qualitative and quantitative results demonstrate the particle size convergence of the δ R-SPH-OPS-VCS-VEM-HPDC schemes in velocity divergence error cleaning.

The effectiveness of the proposed schemes in mitigating spurious pressure fluctuations is quantitatively demonstrated through comparing the results by the models that add the foregoing schemes one by one. Specifically, the time histories of the pressure at the center of the fluid patch predicted by δ R-SPH-OPS-VCS, δ R-SPH-OPS-VCS-VEM and δ R-SPH-OPS-VCS-VEM-HPDC are compared in Fig. 6(a). In spite of the

consistent overall trend for all simulations, i.e., unphysical pressure fluctuations occurring at the early stage and gradually attenuating, the magnitude of fluctuations reduces with the incorporation of the VEM and HPDC schemes. Besides, the predicted pressure history by δ R-SPH-OPS-VCS-VEM-HPDC converges to the BEM-MEL result (at $t\omega = 0.6$) much faster than those by δ R-SPH-OPS-VCS-VEM (at $t\omega = 0.9$) and δ R-SPH-OPS-VCS (at $t\omega = 2.0$). These indicate the effectiveness of the proposed schemes in suppressing pressure noises.

Fig. 6(b) presents the pressure time histories by δ R-SPH-OPS-VCS and δ R-SPH-OPS-VCS with and without VEM-HPDC, the results obtained by these two stabilization terms, i.e., the Riemann stabilization term and the artificial viscosity, are all in a good agreement with the reference solution. Regarding the pressure evolution, the Riemann stabilization term does not bring a significant improvement compared to the artificial viscosity. It is primarily attributed to the relatively uniform particle distributions and the suppression of tensile instability through TIC. However, the enlarged view at $t = 6.0$ s shows that the pressure values predicted by the Riemann stabilization term are slightly higher than those by the artificial viscosity term, which indicates that less energy is dissipated in the center region.

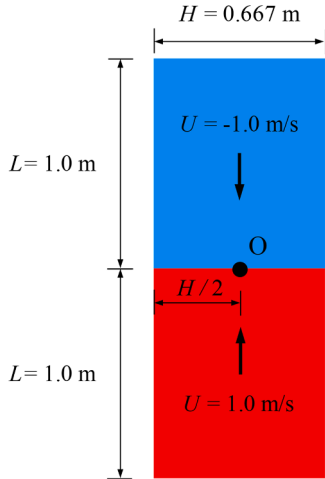


Fig. 8. Schematic view of the impact of two rectangular fluid patches along the longitudinal direction.

The energy conservation property of the Riemann stabilization term is tested based on the resolution of $L/dp = 100$. For the simulation using artificial viscosity, the coefficient α is set to be 0.05 [31,69] for numerical stability. The time histories of normalized kinetic energy by the models $\delta\text{R-SPH-OPS-VCS-VEM-HPDC}$ and $\delta\text{-SPH-OPS-VCS-VEM-HPDC}$ are presented in Fig. 7, where E_k is the kinetic energy at a certain time instant and E_{k0} the energy at the initial stage. As can be seen, the kinetic energy dissipation in the model with artificial viscosity reaches 10.2% at $t\omega = 8.0$, which is 1.7 times more than twice that in the proposed δR model with Riemann stabilization term (5.9%). Besides, the slopes of the curves indicate that the energy dissipation in the $\delta\text{-SPH}$ remains considerable after $t\omega = 8.0$, while that in the $\delta\text{R-SPH}$ model becomes moderate after $t\omega = 7.0$, which is especially helpful in long-term simulations. These demonstrate the superior performance of the Riemann dissipation term in energy conservation.

5.2. Impact of two rectangular fluid patches

Secondly, the normal impact of two rectangular fluid patches characterized by the sudden impact and energy losses [55] is simulated to test the introduced schemes in modeling high-velocity fluid impacts. As depicted in Fig. 8, two identical fluid patches of length $L = 1.0$ m and

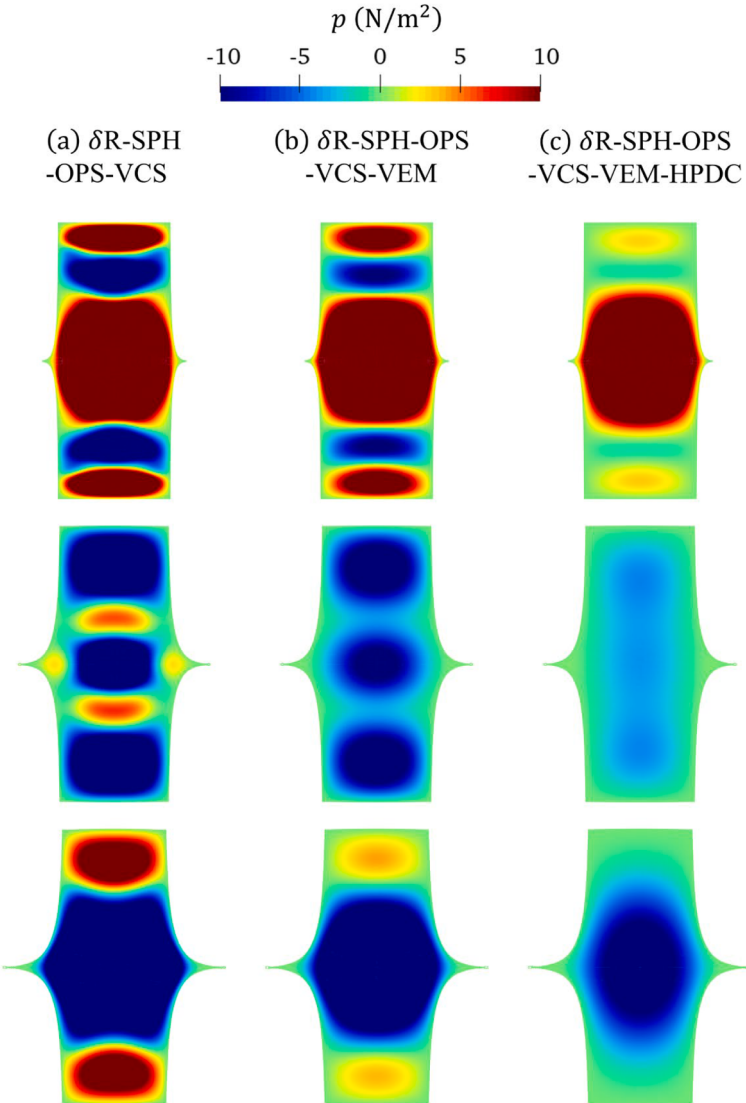


Fig. 9. Pressure contours at $t = 0.03$ s, 0.08 s and 0.12 s predicted by: (a) $\delta\text{R-SPH-OPS-VCS}$; (b) $\delta\text{R-SPH-OPS-VCS-VEM}$; (c) $\delta\text{R-SPH-OPS-VCS-VEM-HPDC}$ - impact of two rectangular fluid patches.

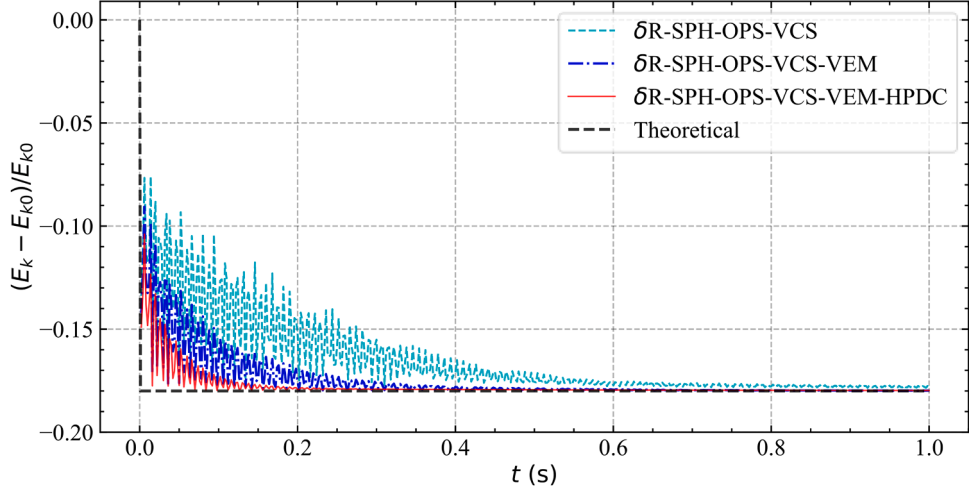


Fig. 10. Time histories of normalized kinetic energy by δ R-SPH-OPS-VCS, δ R-SPH-OPS-VCS-VEM and δ R-SPH-OPS-VCS-VEM-HPDC in comparison with the theoretical solution - impact of two rectangular fluid patches.

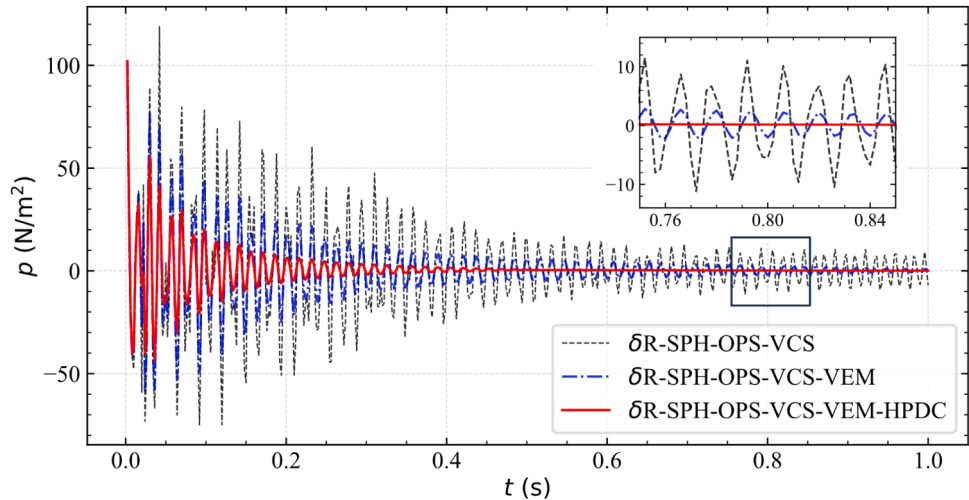


Fig. 11. Pressure histories at the center of the two patches simulated by δ R-SPH-OPS-VCS, δ R-SPH-OPS-VCS-VEM and δ R-SPH-OPS-VCS-VEM-HPDC - impact of two rectangular fluid patches.

width $H = 0.667$ m are subjected to an initial longitudinal approaching velocity $U = 1.0$ m s⁻¹. The impact of the two patches generates strong shock waves, which propagate outward instantaneously. With the assumption of inviscid and incompressible fluids, the impact causes a sudden loss of internal energy in the fluid system that has an exact analytical solution [55,63]. In simulations, for better reproduction of the weakly-compressible fluid regime, the speed of sound is selected as $c_s = 100$ U = 100 m s⁻¹; the fluid density is $\rho = 1$ kg/m³; the Riemann dissipation coefficient is $\beta = 3$; the particle resolution is $dp = 0.005$ m.

To illustrate the effectiveness of the proposed schemes in eliminating pressure noises, the pressure fields predicted by δ R-SPH-OPS-VCS, δ R-SPH-OPS-VCS-VEM and δ R-SPH-OPS-VCS-VEM-HPDC are studied. As presented in Fig. 9, the results by δ R-SPH-OPS-VCS clearly show alternating positive and negative pressures of considerably large amplitudes, which corresponds to the compression and rarefaction of fluid and their propagations in the domain. As shown in columns (b) and (c), the compression/rarefaction waves that are not consistent with the physical process of incompressible or weakly-compressible flows are partially reduced by VEM and further mitigated by the combination of VEM and HPDC.

Fig. 10 demonstrates the performance of the proposed schemes in energy conservation. In theory, the sudden kinetic energy drop upon the

impact corresponds to the energy carried by the shock waves, which propagate outward instantaneously. In SPH simulations, however, the kinetic energy drops last for certain periods and are accompanied by oscillations due to the weak fluid compressibility and the back-and-forth propagations of acoustic waves. More specifically, in δ R-SPH simulations without VEM and HPDC, the kinetic energy drop takes place slowly. By implementing VEM and HPDC, the time histories of the kinetic energy drop manifest smaller oscillations and converge faster to the theoretical solution for incompressible flows. This means that the VEM and HPDC schemes help the mitigation of unphysical noises in pressure or dynamics and improve the imposition of the incompressible condition for fluid.

Fig. 11 depicts the pressure histories at the center of the connection boundary of the two patches, i.e., point O in Fig. 8. Spurious fluctuations exist in the beginning and decay with time in the simulations by δ R-SPH models with different schemes. The adoption of VEM reduces the fluctuations magnitude by 76.9% and a further utilization of the HPDC scheme reduces 11.9% more of the fluctuations (numbers are based on a typical pressure peak period). Consistent with the energy evolution curve, the spurious pressure fluctuations decay the fastest in the δ R-SPH-OPS-VCS-VEM-HPDC simulation. The enlarged view of the pressure values at around $t = 0.8$ s shows that the unphysical pressure

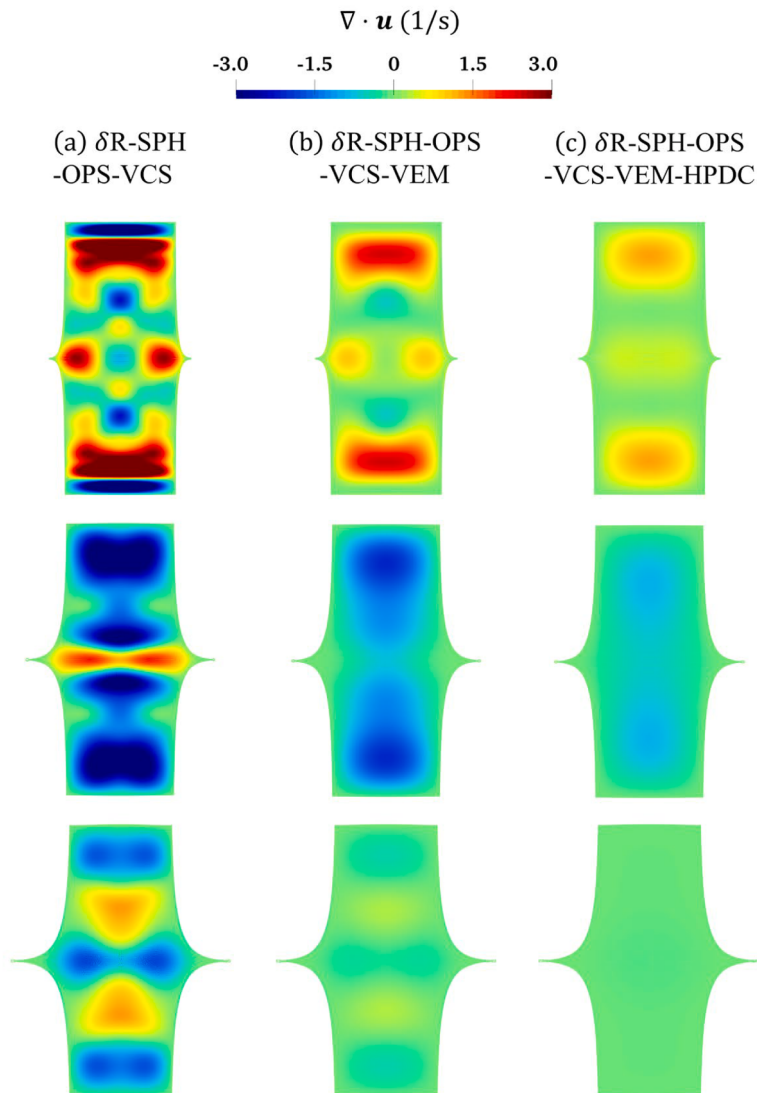


Fig. 12. Snapshots of divergence of velocity fields at $t = 0.03$ s, 0.08 s, 0.12 s by: (a) δ R-SPH-OPS-VCS; (b) δ R-SPH-OPS-VCS-VEM; (c) δ R-SPH-OPS-VCS-VEM-HPDC - impact of two rectangular fluid patches.

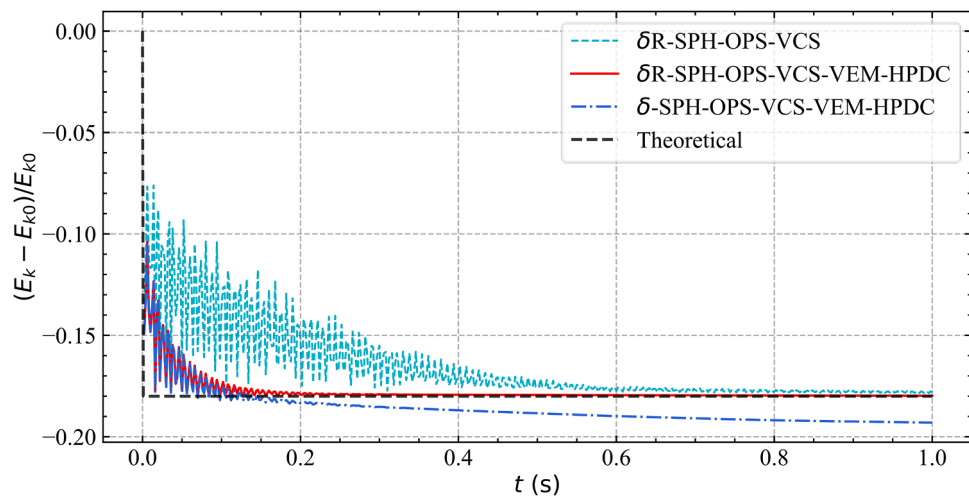


Fig. 13. Time histories of normalized kinetic energy by δ -SPH-OPS-VCS, δ -SPH-OPS-VCS-VEM-HPDC and δ R-SPH-OPS-VCS-VEM-HPDC together with the theoretical solution - impact of two rectangular fluid patches.

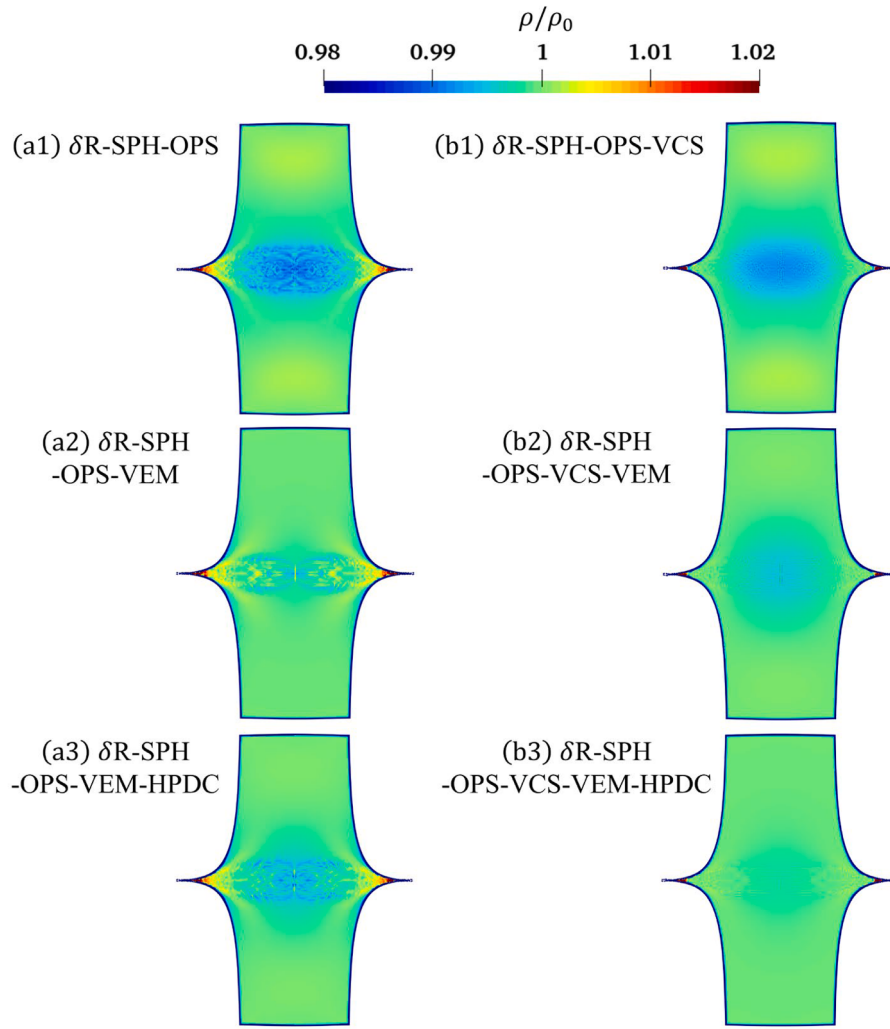


Fig. 14. Particle density contours evaluated by kernel summation at $t = 0.12$ s: (a) without VCS; (b) with VCS - impact of two rectangular fluid patches.

fluctuations have been fully cleaned by the incorporation of the VEM and HPDC schemes, while certain oscillations still exist in the δR -SPH with VEM solely due to the accumulated error in the velocity divergence field. These results demonstrate the advantage of the δR -SPH model enhanced by VEM and HPDC in stabilizing the pressure field and suppressing the acoustic waves in weakly compressible simulations.

The velocity divergence contours at typical time instants simulated

by δR -SPH-OPS-VCS, δR -SPH-OPS-VCS-VEM and δR -SPH-OPS-VCS-VEM-HPDC are compared in Fig. 12. In the baseline results by δR -SPH-OPS-VCS, non-zero velocity divergences of relatively large amplitudes occur in the entire computational domain and their spatial positions change, which correspond to the compression/rarefaction of fluid and the acoustic pressure waves. The utilization of VEM reduces the magnitude of the velocity divergence error by >50% and reduces the

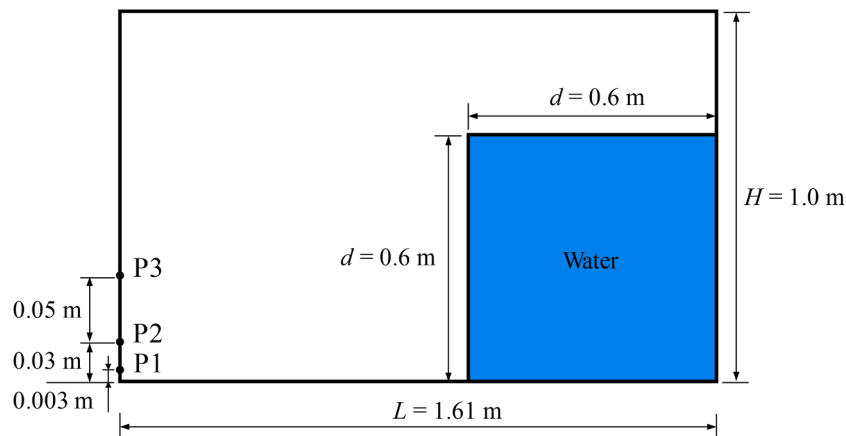


Fig. 15. Computational domain of the case of dam break flow.

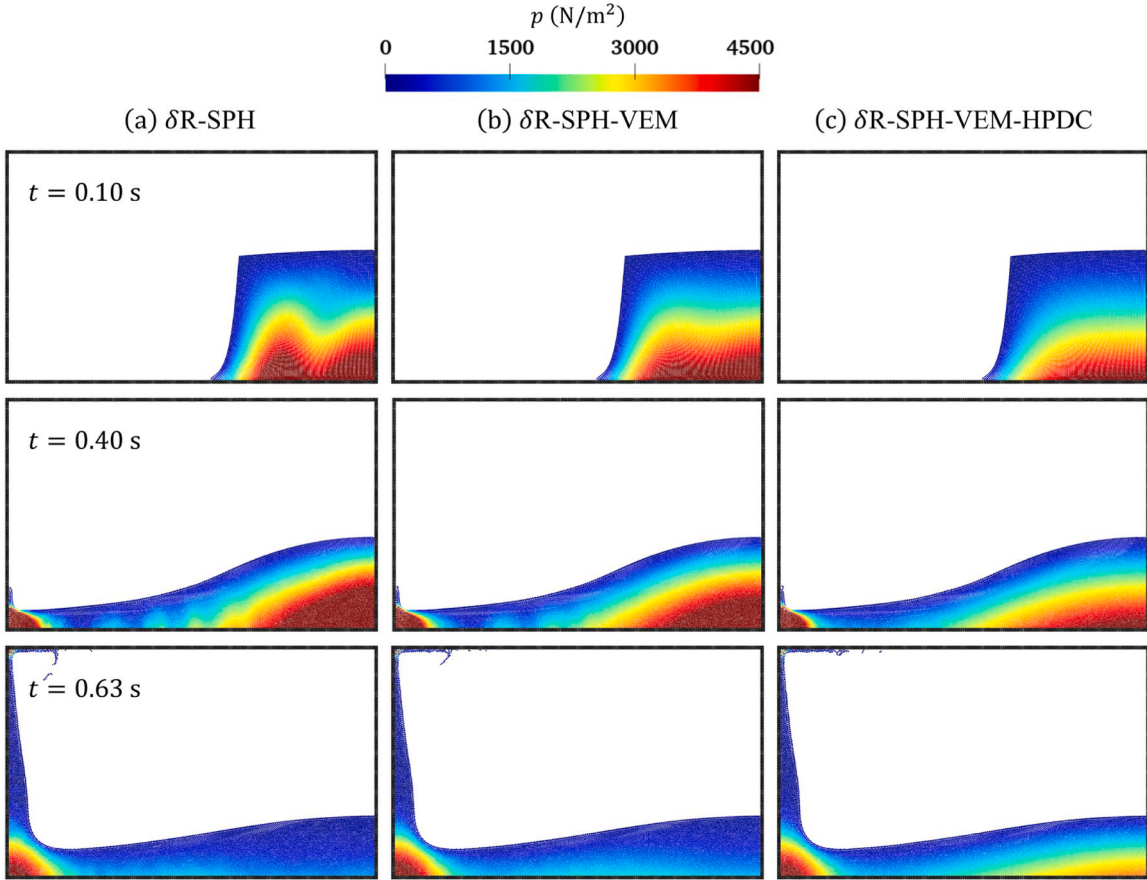


Fig. 16. Snapshots of pressure contours at $t = 0.10$ s, 0.40 s and 0.63 s by: (a) δR -SPH; (b) δR -SPH-VEM; (c) δR -SPH-VEM-HPDC - two-dimensional dam break.

area of regions with significant errors, implying a significant enhancement of the spatial continuity of the velocity divergence field. Further incorporation of HPDC mitigates the non-zero velocity divergence more effectively. Specifically, the velocity divergence is cleaned to almost zero at $t = 0.12$ s, which indicates an enhanced satisfaction of the incompressibility conditions.

Fig. 13 presents the time variations of kinetic energy in three groups of simulations. Before $t = 0.1$ s, the combined actions of VEM and HPDC schemes mitigate a significant portion of the energy dissipation associated with the acoustic waves of weakly compressible fluids (by comparing the results between δR -SPH-OPS-VCS models with and without VEM-HPDC). At this stage, the percentage of the energy dissipation by the Riemann dissipation term or the artificial viscosity is small and hence the results by both models show few differences. After $t = 0.2$ s, most of the compression/rarefaction waves in the flow field have been eliminated, and both the artificial viscosity and the Riemann stabilization term start to make dominating effects in damping noises in a way somewhat similar to the physical viscosity. Specifically, the energy of the fluid system in the artificial-viscosity simulation drops continuously, while that in the Riemann-term simulation conserves and matches well with the analytical solution. This demonstrates the advantage of the δR -SPH model in mitigating spurious noises while not introducing excessive dissipations.

To illustrate the performance of introduced schemes in volume conservation, the kernel summation-based density fields produced by the schemes without and with VCS are compared in Fig. 14. As shown in Fig. 14(a1), the density field by δR -SPH-OPS exhibits evident noise (with magnitude being 4%) and discontinuities in the center and tip regions, which correspond to the unphysical fluid volume expansion and compression and are induced partially by the particle shifting technology. From Fig. 14(a2) and (a3), it can be seen that the density errors and

noises are mitigated by VEM and HPDC schemes due to the effective cleaning of instantaneous and accumulated velocity divergence error, leading to a spatially more continuous density field. The comparison of the left- and right-column contours shows that the VCS scheme effectively mitigates the density errors in the whole domain and achieves better volume conservation. Specifically, the result by the δR -SPH-OPS-VCS-VEM-HPDC model shows marginal deviation from the reference density as shown in Fig. 14(b3). This, combined with the imposition of the velocity divergence field shown in Fig. 12(c3), demonstrates the improved resolution of the continuity equation by the developed VCS, VEM and HPDC schemes.

5.3. Two-dimensional dam break

Thirdly, the dam break case [64,70–72] that involves highly deformed free surfaces and violent impacts is studied to demonstrate the effectiveness of the proposed schemes in mitigating pressure noises when simulating violent free-surface fluid flows. Fig. 15 sketches the computational domain, where the water tank has a length of $L = 1.61$ m and a height of $H = 1$ m, and a square-shaped water bulk of height $d = 0.6$ m is initially deployed and released. Three pressure probes, i.e., P1, P2 and P3, are placed on the left wall of the tank to measure the fluid impact pressures, and their distances to the tank bottom are 0.003 m, 0.03 m and 0.08 m, respectively. In the present simulations, the particle resolution is $dp = 0.004$ m and the numerical speed of sound is $c_s = 20\sqrt{gd}$. The median data of multiple experimental tests as presented in Lobovský et al. [64] are used as the benchmark to demonstrate the performance of the developed SPH model.

The pressure contours predicted by the δR -SPH, δR -SPH-VEM and δR -SPH-VEM-HPDC models at typical time instants are presented in Fig. 16. The flowing flow impacts on the side wall and induces violent fluid

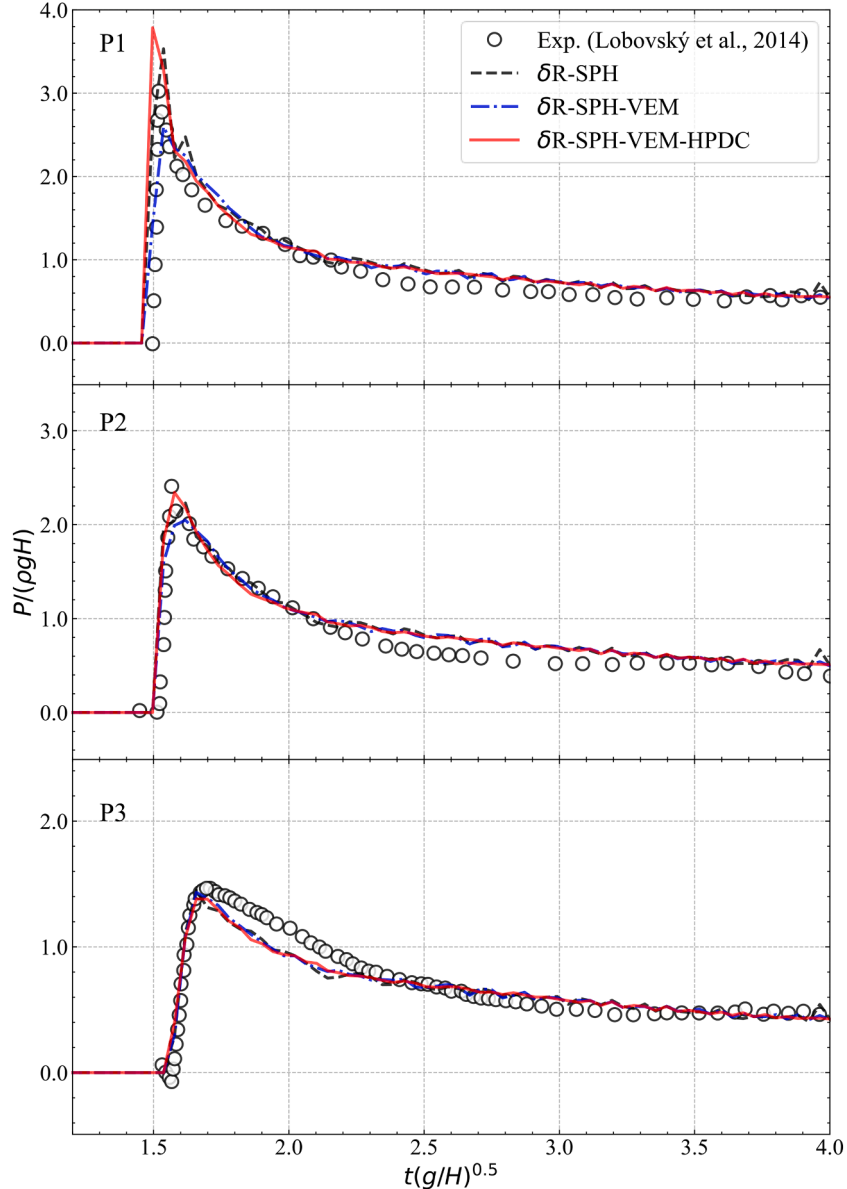


Fig. 17. Pressure time histories at P1, P2 and P3 in comparison with the experimental data - two-dimensional dam break.

pressures in the area around the impact location (see the pressure contours at $t = 0.40$ s). In the framework of weakly compressible simulation, the violent pressures correspond to noticeable changes in fluid density. These, due to the allocated particle interpolation nature, further lead to the alternating local compression and rarefaction of fluids, which are manifested as acoustic pressure waves that propagate outwards and then get reflected by the boundaries. In the δ -SPH simulation, such acoustic waves are evident and contaminate the hydrodynamic pressure field. As can be seen from Fig. 16(b), such noises in the pressure field can be partially removed by the VEM scheme as shown in column (b). Further incorporating the HPDC scheme almost eliminates the acoustic noises and produces more physically consistent pressure fields as shown in Fig. 16(c).

The pressure histories at measurement locations predicted by δ -SPH, δ -SPH-VEM and δ -SPH-VEM-HPDC are presented in Fig. 17. In general, all the numerical models predict the impact pressures satisfactorily well in terms of the peak value and rise time as compared to the experimental results [64]. The pressure history during the impact process predicted by δ -SPH-VEM contains less fluctuations as compared to δ -SPH, and the result becomes even smoother with the further

introduction of HPDC.

The time histories of the system's mechanical energy in simulations by using the artificial viscosity and the Riemann stabilization term are presented in Fig. 18, where E_t and E_{t0} denote the total mechanical energy at time t and the initial state, respectively. Before the flow impact on the wall, the δ -SPH model with artificial viscosity term leads to considerable energy dissipation, while the issue is well addressed by the δ -SPH with the Riemann term. Three energy drops occur at $t = 0.37$ s, 0.55 s and 1.07 s, which correspond to the dam break flow impacting the left wall, impacting the upper wall, and the splashing particles hitting the wall and water body. Compared to artificial viscosity, the Riemann dissipation term can better capture the sudden energy drop caused by the impact process and avoid the issue of excessive energy dissipation. Within the whole simulation process, the mechanical energy drop in the simulation with the Riemann stabilization term was reduced by 114%. These demonstrate the superior features of the δ -SPH in conserving energy.

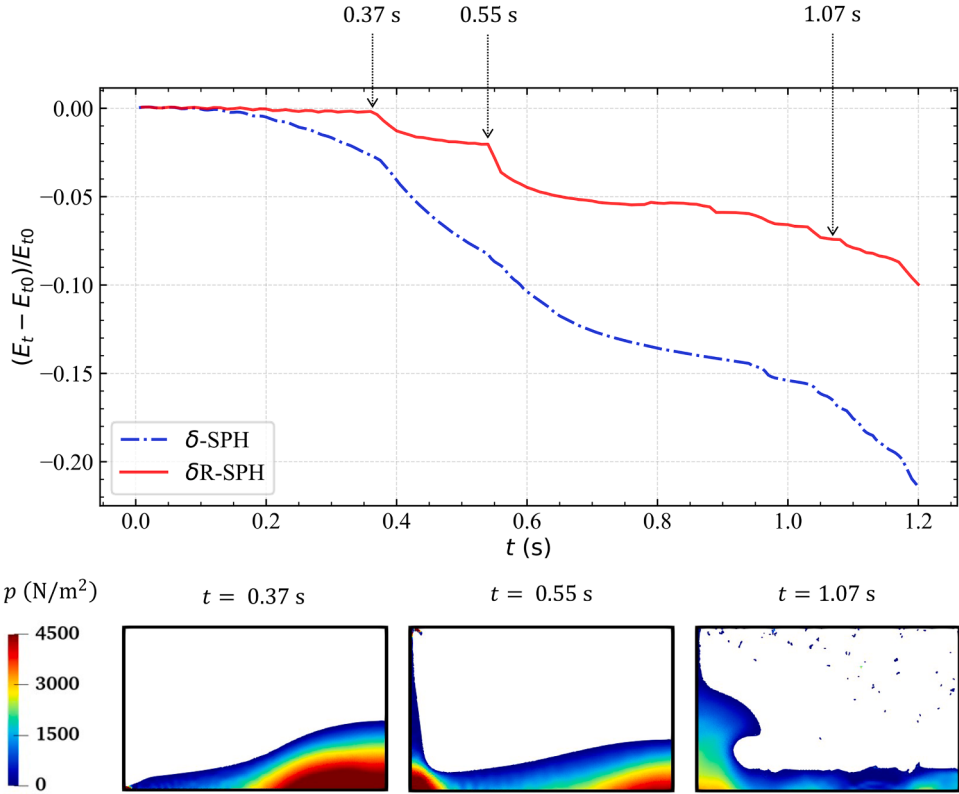


Fig. 18. Time histories of the total mechanical energy of the dam break system and three snapshots by δR -SPH corresponding to the sudden drops of system energy - two-dimensional dam break.

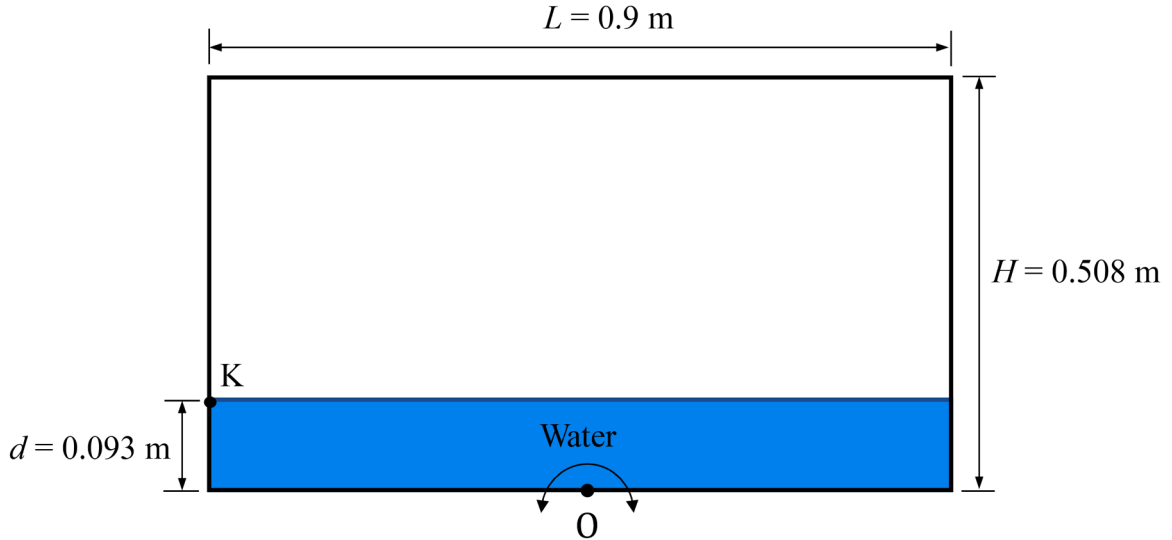


Fig. 19. Schematic view of sloshing under rotational excitation.

5.4. Liquid sloshing under roll excitation

The violent sloshing under rotational excitation [65,73–75] is simulated to verify the accuracy of the proposed schemes in long-term simulation. The computational setup is sketched in Fig. 19, where the tank length L and height H are 0.9 m and 0.508 m, respectively, and the initial water level d is 0.093 m. The tank is under a sinusoidal rotational excitation governed by $\theta(t) = A \sin(2\pi t/T_s)$, where the rotational amplitude is $A = 4^\circ$ and the period is $T_s = 1.6295$ s. The sloshing pressure on the left wall with a distance of 0.093 m (the same as the initial water level) to the tank bottom is measured. In simulations, the

particle resolution is $dp = 0.004$ m and the speed of sound is $c_s = 20\sqrt{gd}$.

The pressure time histories at Point K predicted by δR -SPH, δR -SPH-VEM and δR -SPH-VEM-HPDC are presented in Fig. 20. The key features of all numerical results are in the consistent trend with the experimental data although the pressure peaks are slightly over-predicted, which is presumably attributed to the single-phase simulation ignoring the air effect. By comparing the three sets of numerical results, it can be seen that the unphysical high-frequency pressure oscillations are suppressed by the VEM and further reduced by the incorporation of HPDC. These demonstrate the effectiveness of the VEM and HPDC schemes and

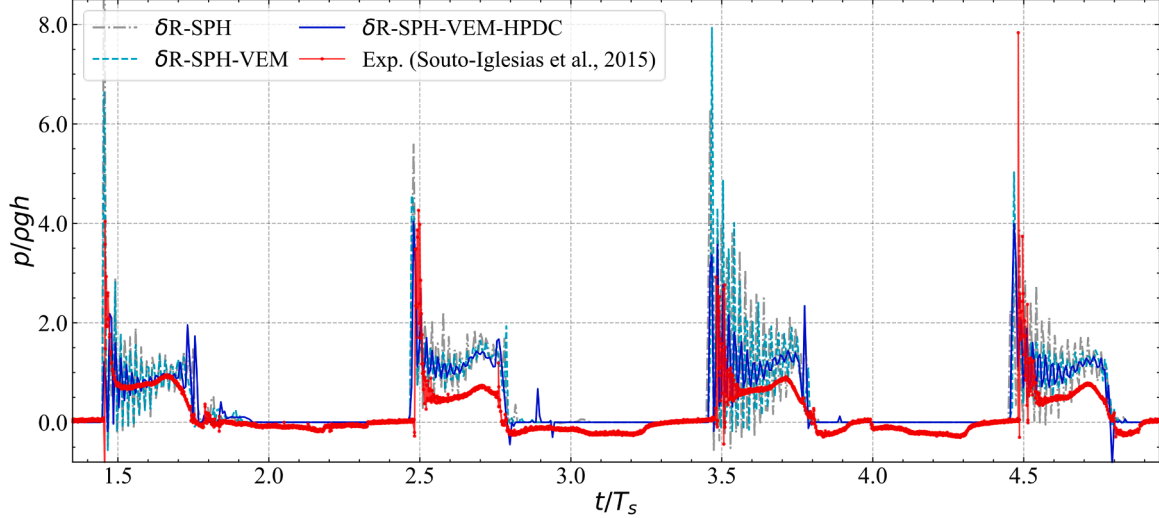


Fig. 20. Pressure time histories by δR -SPH, δR -SPH-VEM and δR -SPH-VEM-HPDC in comparison with the experimental data - liquid sloshing under roll excitation.

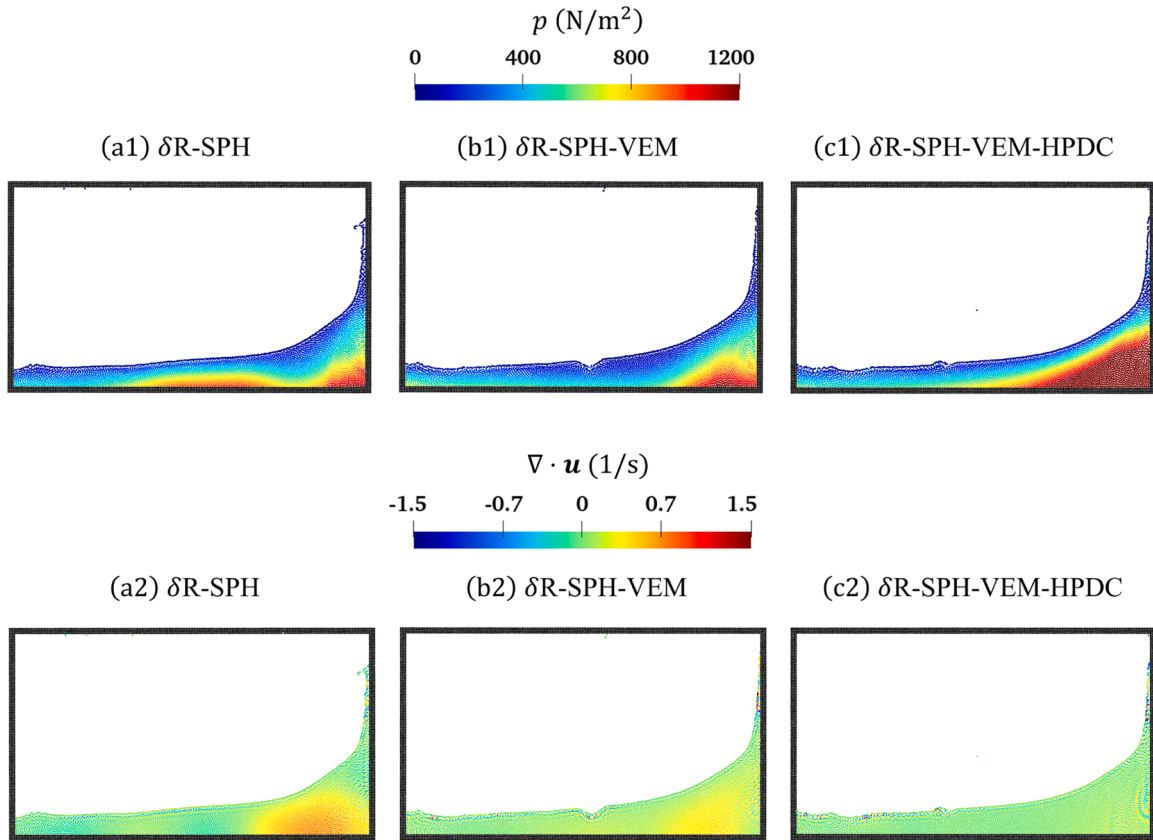


Fig. 21. Fluid particle distributions with contours of pressure and velocity divergence at $t = 8.21$ s simulated by: (a) δR -SPH; (b) δR -SPH-VEM; (c) δR -SPH-VEM-HPDC - liquid sloshing under roll excitation.

especially their combined actions in mitigating spurious pressure noises and fluctuations.

The pressure contours and velocity divergence field at a typical time instant (taking $t = 8.21$ s as an example) predicted by δR -SPH, δR -SPH-VEM and δR -SPH-VEM-HPDC are presented in Fig. 21. From Fig. 21(a1), at the instant when the sloshing flow impacts on the wall, the pressure field generated by δR -SPH is not smooth and the velocity divergence field also exhibits significant noises. The implementation of VEM effectively provides cleaning of the velocity divergence error and hence reduces some acoustic pressure components (see Fig. 21(b1)). However,

it is evident that the acoustic wave components with long wavelengths (which can be clearly seen in animations) cannot be effectively eliminated. Also, it can be seen from Fig. 21(b2) that numerical errors exist in the velocity divergence field near the right bottom corner of the tank. In column (c), the contours with VEM and HPDC show spatially more continuous fields of pressure (c1) and velocity divergence (c2). These aspects indicate that the combined implementation of VEM and HPDC provides physically more consistent velocity divergence fields and, hence, more physical pressure results.

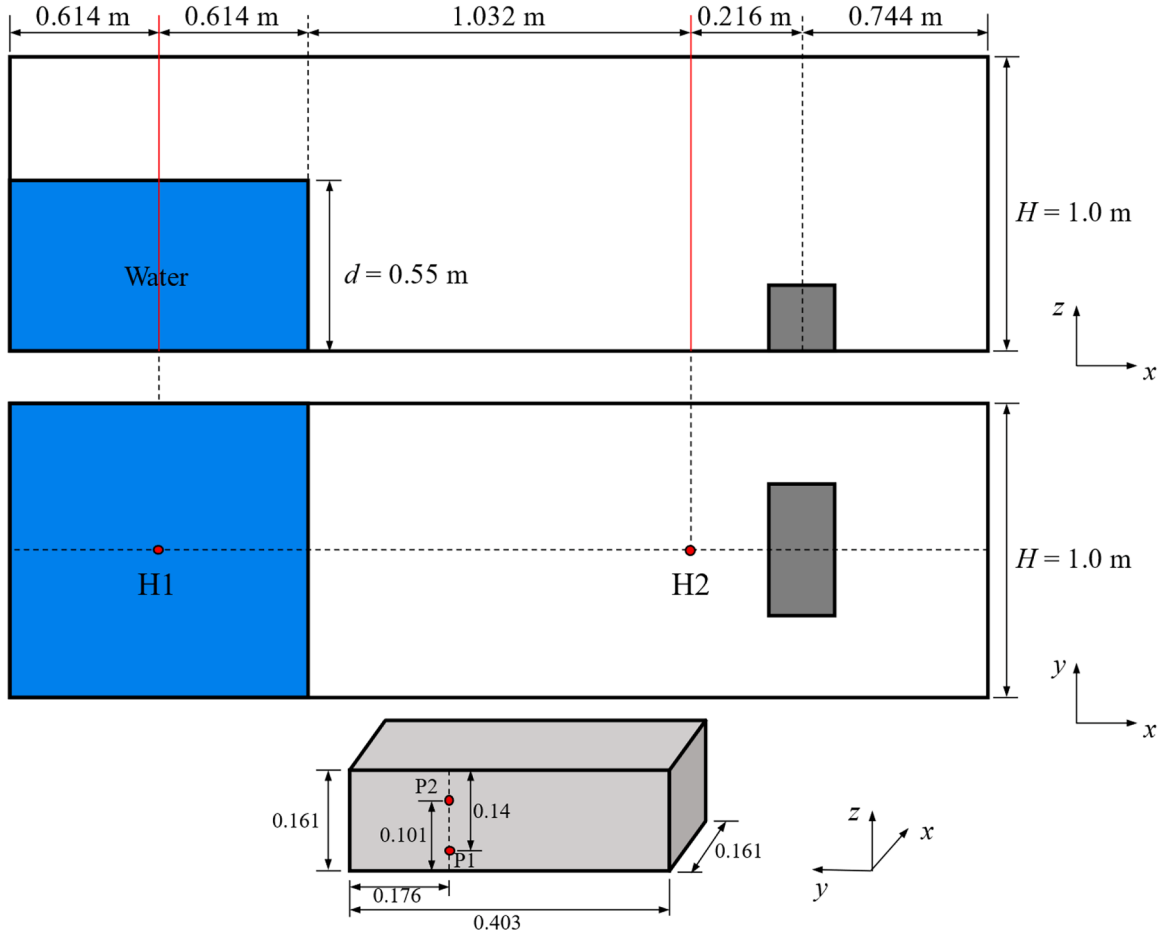


Fig. 22. Schematic view of 3D dam break flow.

— δR -SPH — δR -SPH-VEM	--- δR -SPH-VEM-HPDC ---- Kleefsman, K. M. T., et al., 2005
---	--

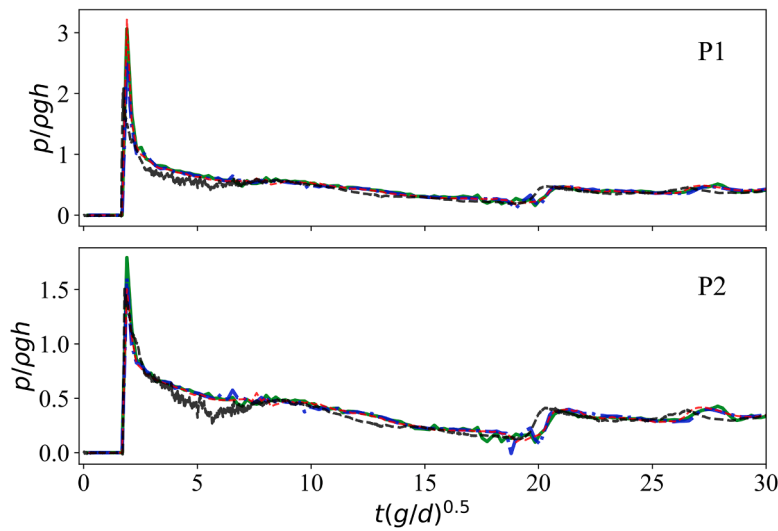


Fig. 23. Pressure time histories at P1, P2 in comparison with the experimental data – three-dimensional dam break.

5.5. Three-dimensional dam break

To demonstrate the effectiveness of the proposed schemes in 3D simulations and to show the performance of the GPU-based implemented version of the proposed schemes, a three-dimensional (3D) dam

break flow impacting a cuboid obstacle [66] is simulated by the GPU-based implemented version of the schemes. Fig. 22 sketches the computational domain. Two pressure probes, i.e., P1, P2 are placed at the front surface of the obstacle to measure the impact pressures. Surface elevations are measured at positions H1, H2. The particle resolution is d_p

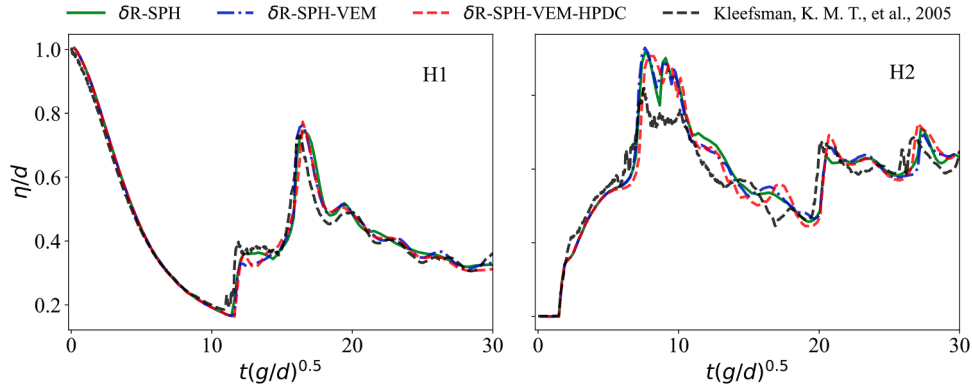


Fig. 24. Free-surface elevation time histories at H1, H2 in comparison with the experimental data – three-dimensional dam break.

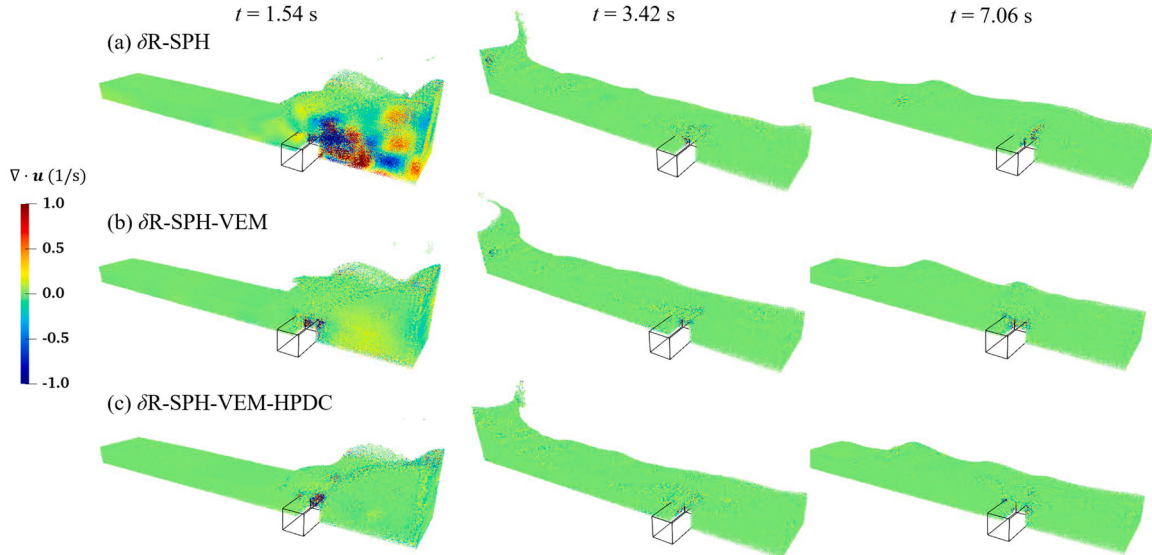


Fig. 25. Snapshots of velocity divergence contours at $t = 1.54$ s, 3.42 s and 7.06 s by: (a) δR-SPH; (b) δR-SPH-VEM; (c) δR-SPH-VEM-HPDC - three-dimensional dam break.

$= 0.01$ m, which gives to about 1.2 million particles. The artificial sound speed is $c_s = 20\sqrt{gd}$.

Fig. 23 presents the pressure histories at measurement locations predicted by δR-SPH-OPS-VCS, δR-SPH-VEM-OPS-VCS and δR-SPH-VEM-HPDC-OPS-VCS. The three sets of numerical results show good qualitative agreement with the experimental data. The peak pressure at P1 is overestimated compared to the experimental data as reported in some previous studies [12,16,76]. It can be also seen that the pressure fluctuations existing in δR-SPH are suppressed by δR-SPH-VEM. The introduction of HPDC further reduces such oscillations and enhances the prediction of the impact pressures. The predicted surface elevation histories at H1 and H2 are presented in Fig. 24, which show satisfactory agreement with the experimental data, demonstrating the capability of DualSPHysics+ in capturing violent 3D free-surface flows.

The velocity divergence contours predicted by the δR-SPH, δR-SPH-VEM and δR-SPH-VEM-HPDC models at three typical time instants are presented in Fig. 25. At $t = 1.54$ s, due to the violent impact of the incident flow on the obstacle, large numerical noises are observed in the results by δR-SPH, which will further cause pressure fluctuations. Such errors are mitigated by the application of VEM and further reduced by the incorporation of HPDC. At later stages of the dam-break flow, e.g., $t = 3.42$ and 7.06 s as shown in the second and third column of the figure, the velocity divergence errors can be observed at the free-surface and wall-vicinity regions in the δR-SPH results. The enhancements of the

velocity divergence field are evident in the results by δR-SPH-VEM and δR-SPH-VEM-HPDC. These achieved results demonstrate the capability of the VEM and HPDC in mitigating the velocity divergence errors and hence in predicting noise-free results.

To demonstrate the effectiveness of introduced schemes in maintaining volume conservation during long-term simulation, the kernel summation-based density fields corresponding to the models without and with OPS, VCS schemes are compared in Fig. 26. The density fields by δR-SPH-VEM-HPDC-OPS (the third row of Fig. 26) exhibit obvious density decrease with time, which implies an unphysical volume expansion induced by OPS. The results by δR-SPH-VEM-HPDC show evident density noises inside the fluid domain, and such noises are effectively suppressed in the results of δR-SPH-VEM-HPDC-VCS, which demonstrate the effectiveness of VCS in maintaining density invariance and volume conservation. In addition, by comparing the results by δR-SPH-VEM-HPDC-VCS and δR-SPH-VEM-HPDC-OPS-VCS, the density errors near the free surfaces are significantly reduced due to the improved particle distribution induced by OPS. The computational performance and memory usage of the GPU codes of the newly added schemes are presented in Appendix A.1.

6. Program documentation

The above-introduced schemes, i.e., the components of the δR-SPH-

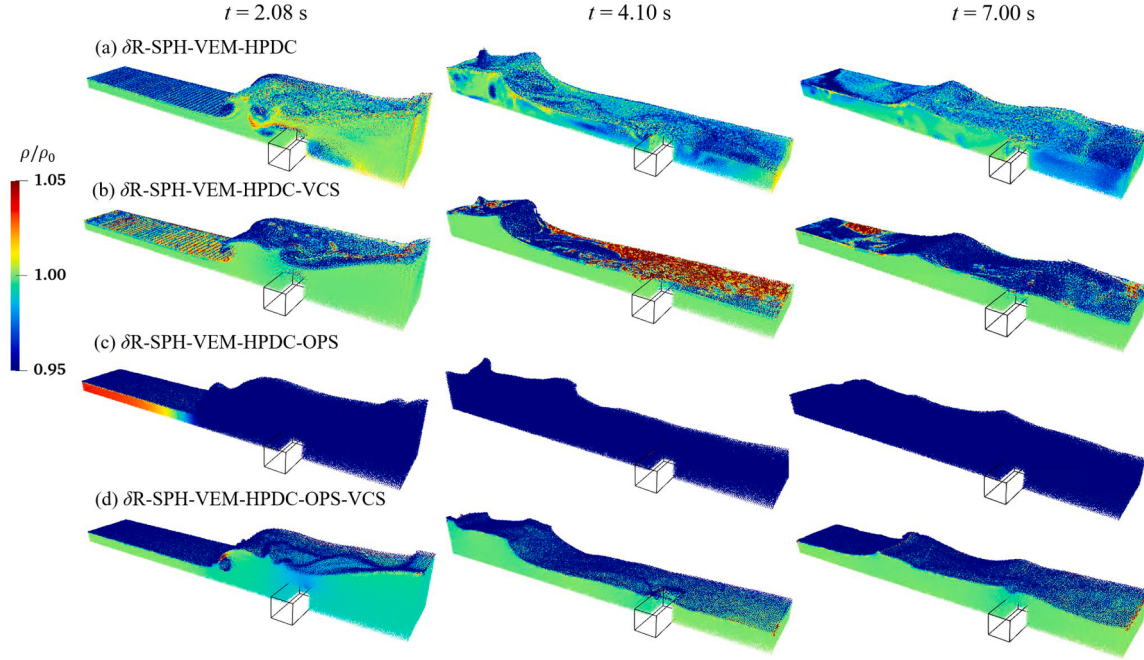


Fig. 26. Particle density contours evaluated by kernel summation simulated by: (a) δR -SPH-VEM-HPDC; (b) δR -SPH-VEM-HPDC-VCS; (c) δR -SPH-VEM-HPDC-OPS; (d) δR -SPH-VEM-HPDC-OPS-VCS - three-dimensional dam break.

Table 2
Added program units of DualSPHysics+ corresponding to the proposed schemes.

Program unit	Categories	Description
JSpHcpu::InteractionForcesFluid KerInteractionForcesFluid	R	Riemann stabilization term based on Eq. (25).
JSpHcpu::RunVEMVCSOPS_StepI KerRunVEMVCSOPS_StepI	VEM	Compute p_a^{VEM} by Eq. (14).
JSpHcpu::RunVEMVCSOPS_StepII KerRunVEMVCSOPS_StepII	VEM	Compute a_d^{VEM} by Eq. (15) and add it into the momentum equation by Eq. (17).
JSpHcpu::InteractionForcesFluid KerInteractionForcesFluid	HPDC	Compute the time derivative of ψ by Eq. (34) and add it to the momentum equation by Eq. (32).
JSpHcpu::ComputeSymplecticPre JSpHcpu::ComputeSymplecticCorr JSpGpu::ComputeSymplecticPre JSpGpu::ComputeSymplecticCorr	HPDC	Update ψ with predictor-corrector time integration scheme.
JSpHcpu:: InteractionForcesBoundDummy KerInteractionForcesBoundDummy	HPDC	Apply the Dirichlet boundary condition for ψ .
JSpHcpu::ShiftFluid KerRunVEMVCSOPS_StepII JSpHShifting::RunOPS	OPS	Compute the Particle Shifting vector by Eq. (13).
JSpHcpu::ComputeSymplecticCorr JSpGpu::ComputeSymplecticCorr	OPS	Apply the Particle Shifting vectors based on Eq. (21).
JSpHcpu::RunVEMVCSOPS_StepI KerRunVEMVCSOPS_StepI	VCS	Compute p^{VCS} by Eq. (19).
JSpHcpu::RunVEMVCSOPS_StepII KerRunVEMVCSOPS_StepII	VCS	Compute δr_d^{VCS} by Eq. (20).
JSpHcpuSingle::GetNormals KerGetNormals	Others	Compute normal vectors of particles based on Eq. (34) of Khayyer et al. [21].
JSpHcpuSingle::FreeSurfaceDetection KerFreeSurfaceDetection	Others	Identify free-surface and free-surface-vicinity particles, inner fluid particles and wall vicinity particles.
JSpHcpu::GetCorrectMatrix KerGetAuxarray	Others	Compute the renormalization matrix for gradient operators.

OPS-VCS-VEM-HPDC model, are implemented in DualSPHysics (V5.2 package), which is an open-source code under the GNU Lesser General Public License (LGPL) [5,40,77,78]. The updated code is termed DualSPHysics+ with several advantageous schemes in enhancements of accuracy, energy conservation, and resolution of the continuity equation. In the following, the implementations of DualSPHysics+ are elaborated.

6.1. Implementations of δR -SPH-OPS-VCS-VEM-HPDC

The proposed schemes are implemented in DualSPHysics in a modular way without affecting the established framework. Table 2 lists the added functions and function templates, as well as the program units categorized according to numerical schemes in both CPU and GPU. Note that most functions are programmed based on the class *JSpHcpu/JSpGpu* and its derived class *JSpHcpuSingle/JSpGpuSingle*, which ensures the portability of the developed schemes.

The functions *JSpHcpuSingle::ComputeStep_Sym* and *JSpGpuSingle::ComputeStep_Sym* implement the Symplectic scheme for time integration in CPU and GPU, respectively. Fig. 27 illustrates the flowchart of one time step computation with the red color indicating the key variables in the added schemes. In the predictor step, the VEM pressure p^{VEM} in Eq. (14), the VEM acceleration a^{VEM} in Eq. (15), the VCS shifting vector δr^{VCS} in Eq. (20), and the OPS shifting vector δr^{OPS} in Eq. (13) are calculated. In the particle interaction process, the boundary conditions for p , u , ψ are imposed; the continuity (Eq. (4)) and momentum (Eq. (32)) equations are solved to get $\frac{Dp}{Dt}$ and $\frac{Du}{Dt}$, respectively; the term $\frac{D\psi}{Dt}$ is computed through Eq. (34). Then, the variables of u , ρ , ψ and r at the intermediate time step, i.e., $k + 1/2$, are updated. Note that a^{VEM} is not added into the solution of the momentum equation in the predictor step.

In the corrector step, the Cell-link list algorithm is implemented to identify the neighboring particles within the supporting radius (typically 2 h). In the process, the arrays storing the physical quantities of particles, including p^{VEM} , δr^{OPS} and δr^{VCS} , are reordered for indexing according to the cell link list. After the particle interaction process (the same as that in the predictor step), a^{VEM} is added into the particle acceleration term through Eq. (17), as well as the shifting vectors δr^{VCS} and δr^{OPS} are used to update particle positions according to Eq. (21).

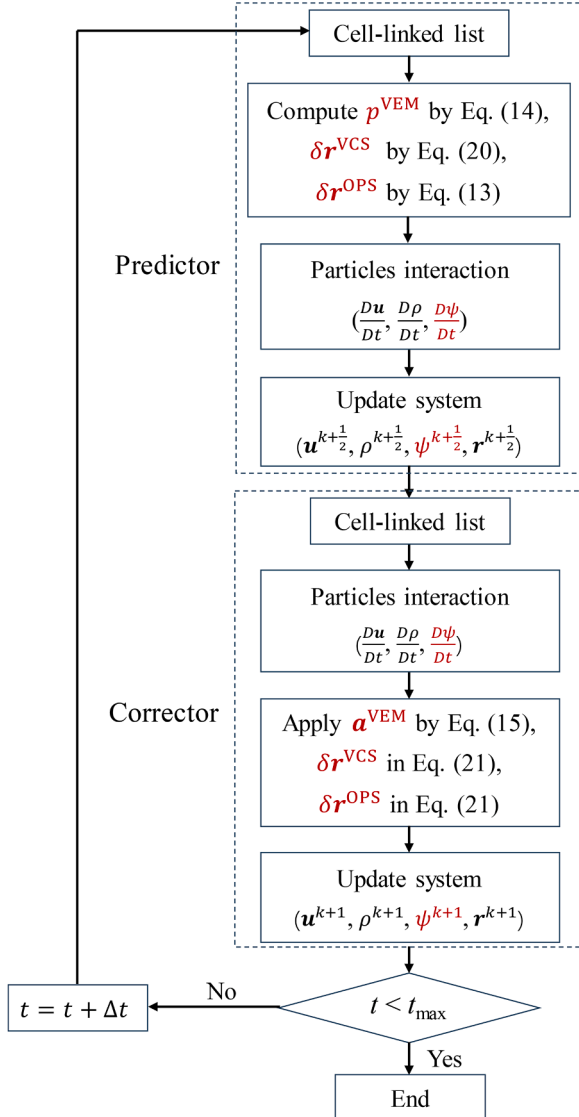


Fig. 27. Computation flowchart of a typical time step in DualSPHysics+ (red color indicates newly added schemes and variables).

6.2. Compiling and running DualSPHysics+

Since there are no additional third-party libraries, the compilation of DualSPHysics+ is similar to that of DualSPHysics. Note that a C++ compiler is necessary for the DualSPHysics+ project (for example GNU's g++ in Linux and Microsoft Visual C++ in Windows). NVIDIA's CUDA Compiler (NVCC) is required for compiling GPU codes. More details on compilation options are referred to Crespo et al. [40].

For each case, one xml (eXtensible Markup Language) file and one sh (Shell) file are provided to run the DualSPHysics+ program. The Case_Def.xml file works as the input file and contains all configurations and numerical parameters for a simulation. One can select the activation of each scheme by setting the value of the corresponding parameter in the xml file. For example, the command `parameter key="Shifting" value="1"` activates OPS in the simulation. The Case_Def.xml is processed into a read-in file by the pre-processing tool GenCase, which is developed together with DualSPHysics and is precompiled in the package [77]. The numerical tests presented in this paper are provided in the folder `/examples/DualSPHysics+` and can be run conveniently with the shell script. For example, case `03_Dambreak` can be launched by the following command: `$ bash xDambreak_linux64_CPU.sh`. Once the

simulation is finished, the script will automatically call the post-processing tools. The output files are in the format of VTK (Visualization Toolkit) and CSV (Comma-separated values) for visualization and data analysis.

7. Concluding remarks

In this paper, an enhanced δ -SPH model with improvements in accuracy, energy conservation and resolution of the continuity equation, abbreviated as δ R-SPH-OPS-VCS-VEM-HPDC, has been proposed. The schemes are implemented in the SPH open-source code DualSPHysics, leading to the DualSPHysics+ for the simulation of incompressible free-surface fluid flows. The enhanced SPH model and code have four enhanced features. Firstly, it applies consistent particle shifting at and in the vicinity of free surfaces by the implementation of OPS. Secondly, the δ R-SPH that integrates the δ -SPH density diffusion term in the continuity equation and a Riemann stabilization term in the momentum equation is proposed, which retains numerical stability, mitigates excessive energy dissipation, and does not bring in possible inconsistencies in the discretized continuity equation (hence volume conservation). Thirdly, the VEM and VCS are incorporated, achieving enhancements in imposing the velocity divergence free and density invariance conditions and thus improving the numerical resolution of the continuity equation. Finally, since the VEM acceleration is just a numerical approximation it may lead to inaccurate estimations when unphysical noises exist in fluid kinematics and thus VEM pressure field, and therefore further contaminate the velocity divergence field. The errors will be accumulated and in turn deteriorate the kinematics. The combination of VEM and HPDC provides a more effective cleaning of both instantaneous and accumulated errors in velocity divergence fields, which further enhances the density and pressure results. The implementations of the introduced schemes, as well as the compiling and running of the DualSPHysics+ code, are elaborated.

The accuracy, energy conservation and enhancement in the resolution of the continuity equation of the developed DualSPHysics+ are validated by five representative benchmark tests with each demonstrating typical aspects of the code. Specifically, the case of a rotating fluid patch shows that the developed code is capable of simulating the large deformation of free surfaces and strong negative pressures, which demonstrates the effectiveness and accuracy of the OPS and TIC schemes. The results also show the good particle spacing convergence of the δ R-SPH-OPS-VCS-VEM-HPDC model in reproducing the fluid kinematics and dynamics. In the case of fluid patches' impact, the nearly divergence-free velocity fields and invariant density fields by DualSPHysics+ indicate the enhanced resolution of the continuity equation and, hence, an improved imposition of the incompressibility conditions. The predicted pressure histories in the dam break case are in good agreement with the published experimental data; further analysis of the energy dissipation demonstrates the superior energy conservation property of the proposed δ R-SPH compared to the artificial viscosity term. In the last case of violent sloshing, the enhancements of velocity divergence and pressure fields portray the capability of VEM and HPDC in mitigating the velocity divergence errors and pressure noises.

Followed by more than a decade of continued efforts by its developers, DualSPHysics has been established as a competent computational code that can simulate a wide range of problems, ranging from fluid mechanics to multi-physics problems [5]. The enhancements presented in this paper are expected to make the enhanced DualSPHysics, i.e., DualSPHysics+, further robust in presenting more physically consistent and reliable solutions corresponding to incompressible fluid flows, including incompressible fluid-structure interactions. Further extensions of the incorporated schemes, for instance, for incompressible-compressible water-air interactions and multi-physics water-air-structure interactions, are among our future works.

CRediT authorship contribution statement

Yi Zhan: Writing – review & editing, Writing – original draft, Visualization, Validation, Software, Resources, Methodology, Investigation, Formal analysis, Data curation. **Min Luo:** Writing – review & editing, Writing – original draft, Supervision, Software, Resources, Project administration, Methodology, Investigation, Funding acquisition, Formal analysis, Conceptualization. **Abbas Khayyer:** Writing – review & editing, Writing – original draft, Supervision, Software, Project administration, Methodology, Investigation, Formal analysis, Conceptualization.

Declaration of competing interest

The authors declare that they have no known competing financial interests or personal relationships that could have appeared to influence the work reported in this paper.

Data availability

The authors have shared the code (with which the data can be

reproduced) at the Attach File step.

Acknowledgement

This research was partially supported by the National Key R&D Program of China (Grant No. 2023YFC3081300), the National Natural Science Foundation of China (Grant No. 12302319), and the Science Foundation of Donghai Laboratory (No. DH-2022KF0311). The authors are grateful to the developers of the open-source DualSPHysics code. Incorporation of the HPDC scheme is inspired by reference [25] and the last author of this paper, Abbas Khayyer is grateful to Dr Georgios Fournakas, the first author of reference [25] for discussions regarding this scheme. The authors appreciate the technical support from the HPC Center of Zhejiang University at Zhoushan Campus. Last but not least, the authors would like to express their sincere appreciation to the anonymous reviewers for their thorough reviews and constructive comments.

Supplementary materials

Supplementary material associated with this article can be found, in the online version, at [doi:10.1016/j.cpc.2024.109389](https://doi.org/10.1016/j.cpc.2024.109389).

Appendix A

A.1. Computational efficiency and memory usage of the newly incorporated schemes

To investigate the computational efficiency and memory usage of the newly incorporated schemes, the computational time per time step, as well as the computational time of one physical second and the memory consumption for the simulation are studied. The simulations are conducted on a micro workstation equipped with AMD Ryzen™ Threadripper™ PRO 5975WX CPU (32 Cores 64 Threads 4.5 GHz), 128 GB RAM and Nvidia RTX™ 3090 Ti (24GB, 10,752 CUDA Cores). The total time steps in different simulations vary slightly due to the variable Δt . As shown in Table 3, based on the two-dimensional dam break case with 27,473 particles, the δR , OPS, VCS, VEM and HPDC schemes increase the computational time by 1.9%, 34.7%, 6.2%, 5.8% and 8.9% comparing to the δ -SPH, respectively. Among the newly implemented schemes, the OPS results in a larger increase in CPU time because of the identification and ad-hoc treatments for the free-surface and free-surface-vicinity particles. More specifically, the proposed δR and the combination of VEM and HPDC schemes lead to 16.6% increase in computational time. The δR , OPS, VCS, VEM and HPDC lead to slight increases in memory consumption, the increased proportion of which are 1.1%, 4.7%, 8.2%, 8.2% and 3.4%, respectively. Note that the overall trends of increased computational time and memory consumption are similar in simulations involving different particle numbers.

Table 3

CPU time and memory usage of SPH models with different schemes in the case of two-dimensional dam break (27,473 particles).

	Total steps	CPU time (s)	CPU time per step (s)	CPU time per physical second (s)	Memory usage (MB)
δ -SPH	32,670	385.5	0.012	321.2	9.0
δR -SPH	32,693	393.0	0.012	327.5	9.1
δR -SPH-OPS	37,063	526.8	0.014	439.0	9.5
δR -SPH-OPS-VCS	35,056	550.8	0.016	459.0	10.3
δR -SPH-OPS-VCS-VEM	34,389	573.3	0.017	477.7	11.0
δR -SPH-OPS-VCS-VEM-HPDC	35,380	607.9	0.017	506.6	11.3

The computational time and memory usage of the GPU codes are tested based on the three-dimensional dam break case presented in Section 5.5. A total number of 1160,663 particles are used and simulations of one second of physical time are conducted. As shown in Table 4, compared to the original δ -SPH model, the δR , OPS, VCS, VEM and HPDC schemes increase the computational time by 4.4%, 42.5%, 16.7%, 7.2% and 3.7%, respectively. The percentages of the increased memory consumption are 3.9%, 5.2%, 8.3%, 5.2% and 3.9%, respectively. Note that the GPU codes including OPS and VCS result in larger increases in computational time compared to the CPU codes because the double-precision (FP64) performance of the accessible hardware is 1/64 of the single-precision (FP32) performance.

Table 4

GPU time and memory usage of SPH models with different schemes in the case of 3D dam break (1160,663 particles).

	Total steps	GPU time (s)	GPU time per step (s)	GPU time per physical second (s)	GPU Memory usage (MB)
δ -SPH	14,914	629.7	0.042	629.7	340.9
δR -SPH	14,825	657.3	0.044	657.3	354.2
δR -SPH-OPS	14,649	924.9	0.063	924.9	371.9
δR -SPH-OPS-VCS	14,709	1030.0	0.070	1030.0	400.4
δR -SPH-OPS-VEM	14,425	1075.3	0.075	1075.3	418.1
δR -SPH-OPS-VEM-HPDC	14,443	1098.5	0.076	1098.5	431.4

A.2. Individual accuracy enhancements by the OPS and the HPDC schemes

The individual enhancing effects by the OPS as well as the HPDC schemes are discussed in detail in this appendix. The OPS does not only enhance the stability and accuracy by its efficient particle regularization effect, but it also enhances the resolution of the continuity equation by providing more spatially continuous density and velocity divergence fields, and by mitigating possible noise in these two fields that may arise, especially in fluid impact test cases. Fig. 28 shows a comparison between δR -SPH and δR -SPH-OPS in the fluid patch impact test. As can be seen, the enhancing effect of the OPS scheme in providing a spatially continuous velocity divergence field is evident. Besides, particle clustering and voids are observed in the enlarged view of the results by δR -SPH. The particles move in a purely Lagrangian manner, which may lead to inaccurate estimation of physical qualities. Moreover, there is a non-physical discontinuity in the jet particles in the results of δR -SPH, which is improved by the δR -SPH-OPS, demonstrating that the OPS significantly enhances the spatial continuity of particle distribution.

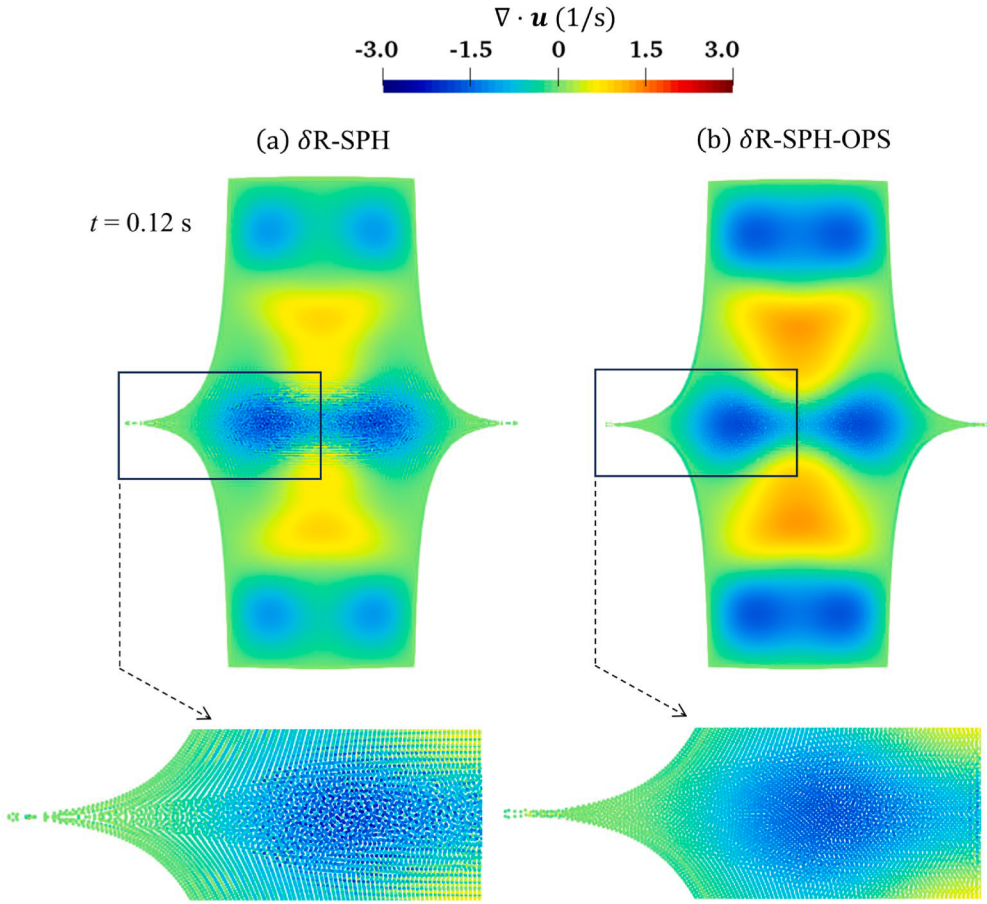


Fig. 28. Snapshots of velocity divergence field at $t = 0.12$ s by: (a) δR -SPH (b) δR -SPH-OPS - impact of two rectangular fluid patches.

The performance of the HPDC scheme in enhancing the numerical resolution of the continuity equation without the VEM scheme is also studied based on the fluid patch impact case. Fig. 29 shows the fluid particles together with the pressure contours at typical time instants. The comparison between the results in columns (b) and (c) shows that HPDC is effective in reducing the unphysical expansion and compression waves. Meanwhile, the combination of VEM and HPDC further cleans the high-frequency noises in the pressure field and hence enhances the satisfaction of the incompressibility conditions. The comparison of the velocity divergence field presented in Fig. 30 demonstrates that the adoption of HPDC provides a reduction of velocity divergence error, yet errors still exist in the center of the patches (see the enlarged view at $t = 0.12$ s).

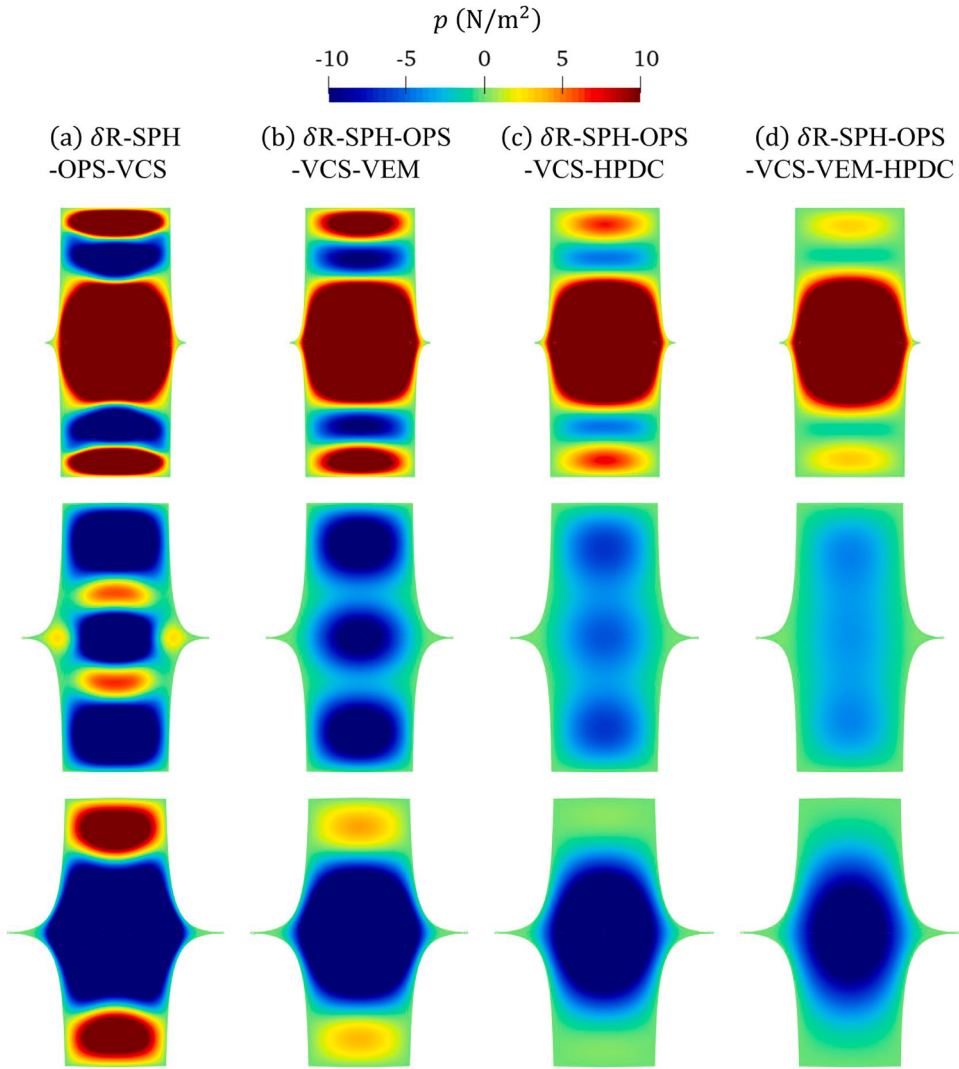


Fig. 29. Snapshots of pressure fields at $t = 0.03$ s, 0.08 s, 0.12 s by: (a) δR -SPH-OPS-VCS; (b) δR -SPH-OPS-VCS-VEM; (c) δR -SPH-OPS-VCS-HPDC; (d) δR -SPH-OPS-VCS-VEM-HPDC - impact of two rectangular fluid patches.

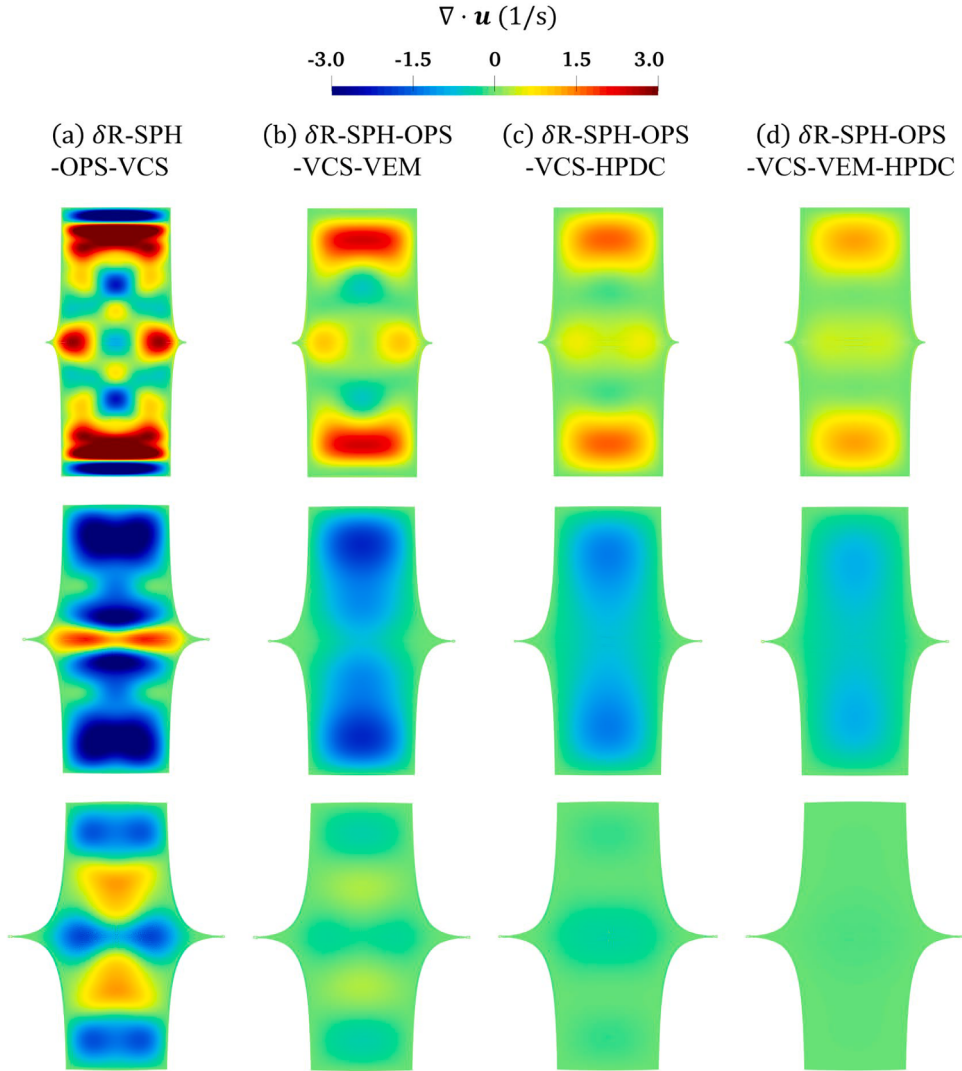


Fig. 30. Snapshots of velocity divergence fields at $t = 0.03$ s, 0.08 s, 0.12 s by: (a) $\delta\text{R-SPH-OPS-VCS}$; (b) $\delta\text{R-SPH-OPS-VCS-VEM}$; (c) $\delta\text{R-SPH-OPS-VCS-HPDC}$; (d) $\delta\text{R-SPH-OPS-VCS-VEM-HPDC}$ - impact of two rectangular fluid patches.

Fig. 31 presents the time histories of the kinetic energy in the results of $\delta\text{R-SPH-OPS-VCS-VEM}$, $\delta\text{R-SPH-OPS-VCS-HPDC}$ and $\delta\text{R-SPH-OPS-VCS-VEM-HPDC}$. All the results show satisfactory energy conservation due to the Riemann stabilization term. At the early stage of the problem (i.e., before $t = 0.2$ s), the curve of $\delta\text{R-SPH-OPS-VCS-HPDC}$ shows less fluctuations than $\delta\text{R-SPH-OPS-VCS-VEM}$. The curve of $\delta\text{R-SPH-OPS-VCS-VEM-HPDC}$ converges to the theoretical solution the fastest, indicating that the combination of VEM and HPDC leads to more effective elimination of the energy associated with fluid compressibility and acoustic waves. Note that the results of $\delta\text{R-SPH-OPS-VCS-HPDC}$ converge to the theoretical solution after $t = 0.4$ s, implying that the HPDC scheme does not introduce excessive numerical dissipations.

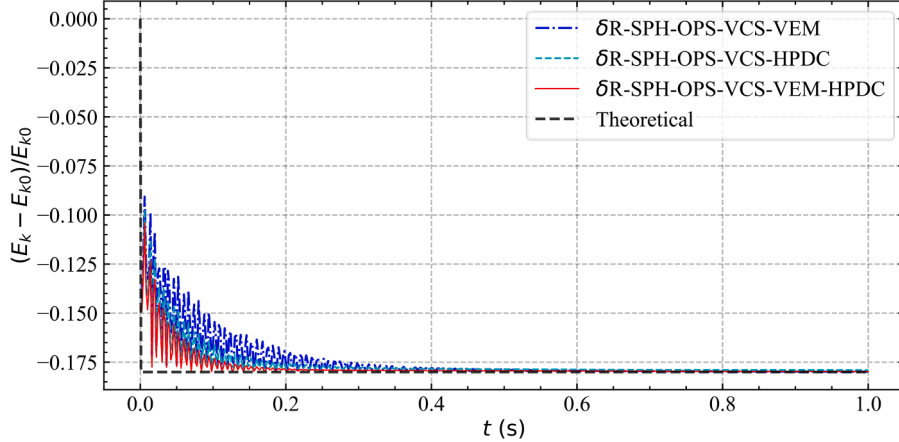


Fig. 31. Time histories of normalized kinetic energy by $\delta R\text{-SPH-OPS-VCS-VEM}$, $\delta R\text{-SPH-OPS-VCS-HPDC}$, $\delta R\text{-SPH-OPS-VCS-VEM-HPDC}$ in comparison with the theoretical solution - impact of two rectangular fluid patches.

A.3. VEM based on the projection concept

In the VEM scheme proposed by Khayyer et al. [21], a pressure term (denoted as p^{VEM^I} here) is explicitly solved based on the equation of state by linking the error in instantaneous velocity divergence to the undesired fluctuations in density over time. Despite its effectiveness in minimizing the velocity divergence errors, the velocity divergence field may not become completely noise-free due to the associated approximations of the velocity divergence field, especially in the vicinity of truncated kernel domains. Inspired by the concept of projection-based particle methods, a secondary corrective pressure for further minimization of velocity divergence error can be derived by projecting the instantaneous velocity field onto a velocity divergence space, which leads to a PPE as follows:

$$\left\{ \nabla \cdot \left(\frac{\nabla p^{\text{VEM}^I}}{\rho} \right) \right\}_a^{k+1} = \frac{\langle \nabla \cdot \mathbf{u} \rangle_a^k}{\Delta t} \quad (36)$$

where p^{VEM^I} represents the secondary corrective pressure. The acceleration associated with this secondary pressure tends to compensate the velocity divergence-free errors. Note that the PPE involving p^{VEM^I} is solved explicitly and thus in a computationally efficient manner similar to that corresponding to p^{VCS} . After the computation of p^{VEM^I} , the acceleration component $\mathbf{a}_a^{\text{VEM}^I}$ can be obtained through Eq. (15). It should be noted here p^{VEM^I} corresponds to a small corrective pressure field and thus, errors linked with approximations associated with explicit solution of the corresponding PPE are deemed to be negligible, in comparison to, e.g., an explicit ISPH computation. Furthermore, this secondary corrective pressure and associated acceleration can be computed and applied at certain time intervals and not necessarily at every computational time step depending on the desired level of the accuracy of velocity divergence field.

To investigate the effectiveness of VEM^{II} in velocity divergence error cleaning, the rotating fluid square is simulated by $\delta R\text{-SPH-OPS}$ incorporated with VEM^I , VEM^{II} and the combination of VEM^I and VEM^{II} (abbreviated as VEM^{III}). In VEM^{III} , the accelerations obtained from VEM^I , VEM^{II} are simply superimposed and applied to the system. The velocity divergence fields at $t\omega = 2.0$ and quantitative velocity divergence errors by three different particle resolutions are presented in Figs. 32 and 33. It can be seen that the velocity divergence errors decrease significantly as the particle resolution increases, which demonstrates the good convergence of the proposed schemes. From the enlarged view of Fig. 32, the VEM^{II} and VEM^{III} appear to be more effective in velocity divergence error cleaning compared to VEM^I , especially at and in the vicinity of free surfaces. Fig. 33 shows a quantitative presentation of averaged velocity divergence error time evolution. It can be also seen from this figure that the utilization of VEM^{II} is slightly more effective in the mitigation of velocity divergence error and combining VEM^I and VEM^{II} tends to further minimize this error.

The energy conservation property of VEM^{II} in comparison with VEM^I and VEM^{III} is tested by three different particle resolutions. The time histories of the normalized kinetic energy by $\delta R\text{-SPH-OPS-VEM}^I$, $\delta R\text{-SPH-OPS-VEM}^{\text{II}}$ and $\delta R\text{-SPH-OPS-VEM}^{\text{III}}$ are shown in Fig. 34. As can be seen, VEM^{II} and VEM^{III} are more dissipative than VEM^I at lower resolutions. With the refinement of particle resolution, VEM^{III} and VEM^I result in almost the same level of energy conservation, indicating that the combination of VEM^I and VEM^{II} is effective in minimizing the velocity divergence error without excessive dissipations, especially in fine-resolution cases.

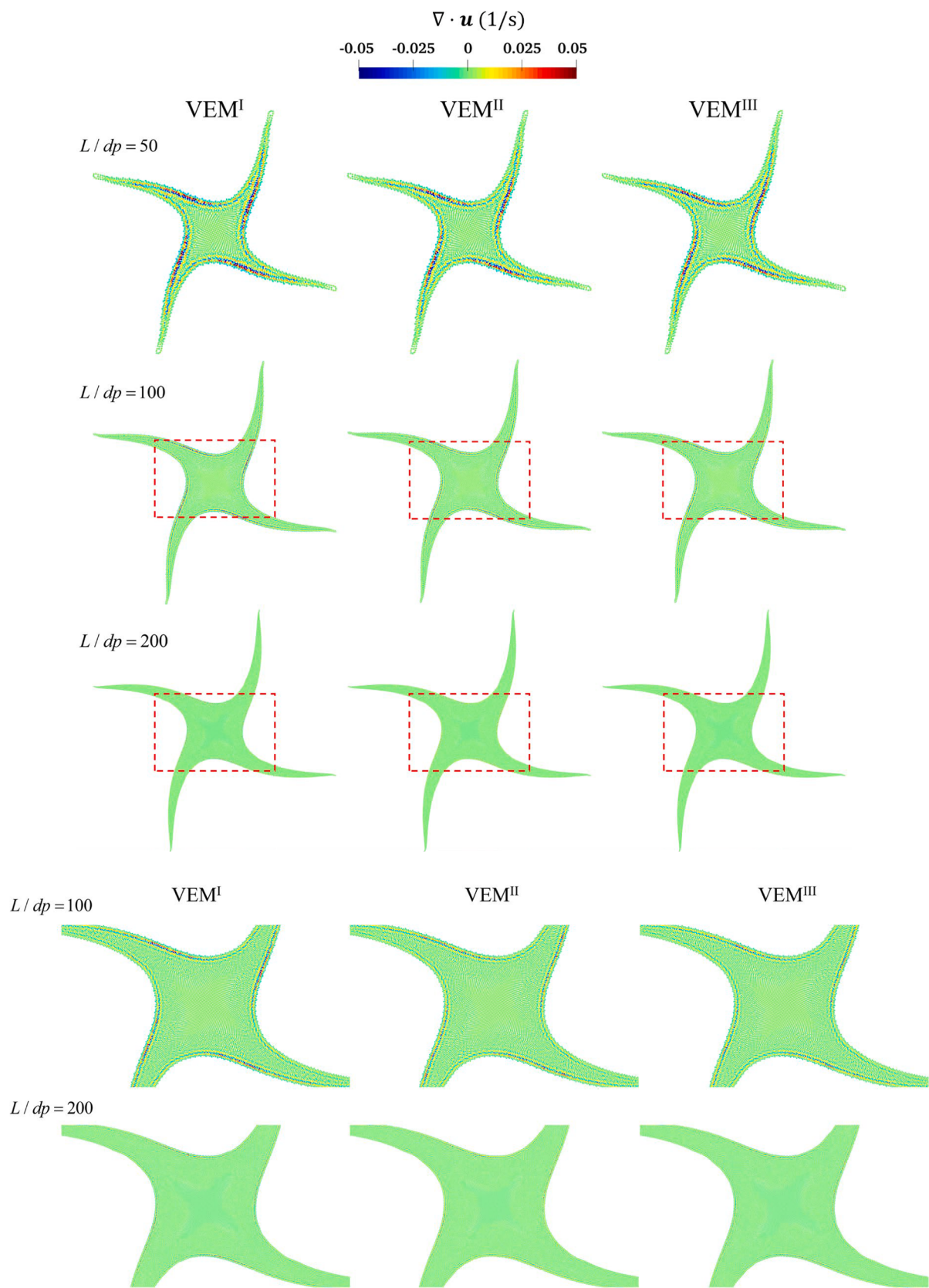


Fig. 32. The velocity divergence contours at $tw = 2.0$ simulated by: VEM^I , VEM^{II} and VEM^{III} corresponding to three different particle resolutions.

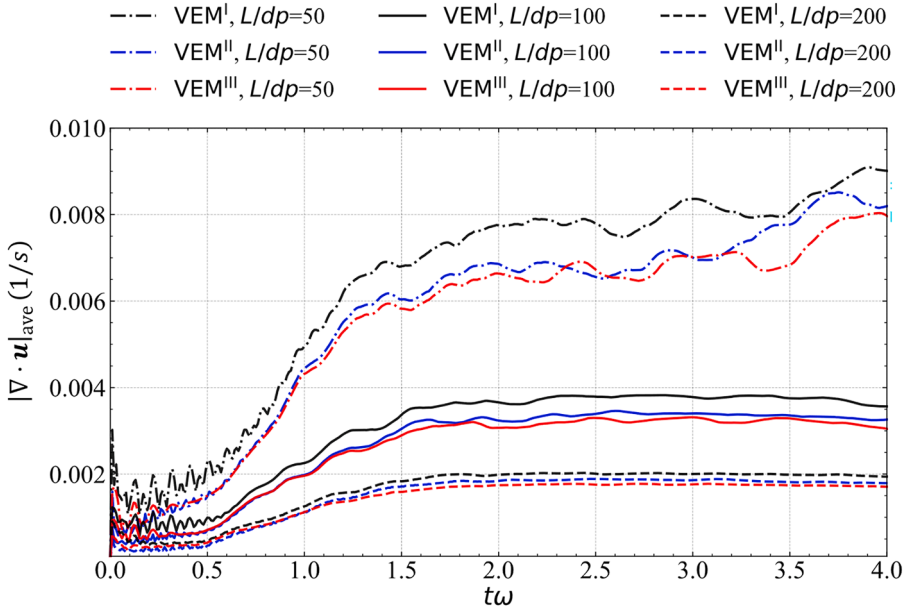


Fig. 33. Time histories of the average absolute value of the velocity divergence error by VEM^I, VEM^{II} and VEM^{III} corresponding to three different particle resolutions.

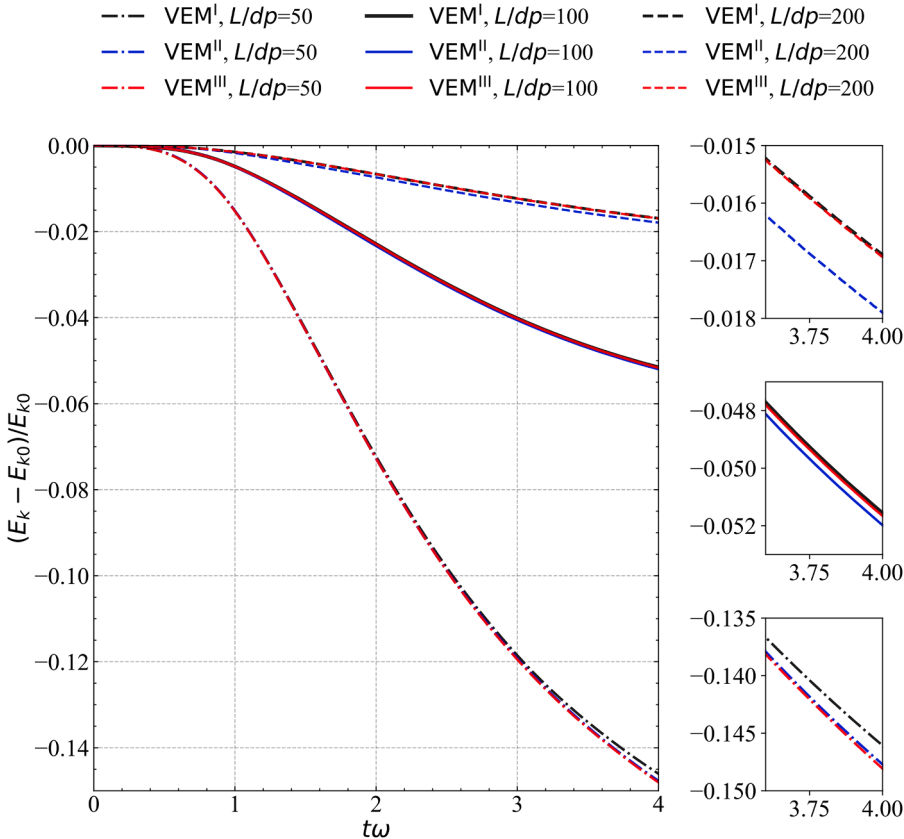


Fig. 34. Time histories of normalized kinetic energy simulated by VEM^I, VEM^{II} and VEM^{III} corresponding to three different particle resolutions.

References

- [1] M.B. Liu, G.R. Liu, Smoothed particle hydrodynamics (SPH): an overview and recent developments, *Arch. Comput. Methods Eng.* 17 (2010) 25–76.
- [2] M. Luo, A. Khayyer, P.Z. Lin, Particle methods in ocean and coastal engineering, *Appl. Ocean Res.* 114 (2021) 102734.
- [3] H. Gotoh, A. Khayyer, Y. Shimizu, Entirely Lagrangian meshfree computational methods for hydroelastic fluid-structure interactions in ocean engineering—Reliability, adaptivity and generality, *Appl. Ocean Res.* 115 (2021) 102822.
- [4] F. Xu, J.Y. Wang, Y. Yang, L. Wang, Z. Dai, R.Q. Han, On methodology and application of smoothed particle hydrodynamics in fluid, solid and biomechanics, *Acta Mech. Sin.* 39 (2023) 722185.
- [5] J.M. Domínguez, G. Fourtakas, C. Altomare, R.B. Canelas, A. Tafuni, O. García-Feal, I. Martínez-Estevez, A. Mokos, R. Vacondio, A.J.C. Crespo, B.D. Rogers, P.

- K. Stansby, M. Gómez-Gesteira, DualSPHysics: from fluid dynamics to multiphysics problems, *Comput. Part. Mech.* 9 (2022) 867–895.
- [6] C. Zhang, M. Rezavand, Y.J. Zhu, Y.C. Yu, D. Wu, W.B. Zhang, J.H. Wang, X.Y. Hu, SPHinXsys: an open-source multi-physics and multi-resolution library based on smoothed particle hydrodynamics, *Comput. Phys. Commun.* 267 (2021) 108066.
- [7] P.N. Sun, A. Colagrossi, S. Marrone, A.M. Zhang, The 8plus-SPH model: simple procedures for a further improvement of the SPH scheme, *Comput. Methods Appl. Mech. Eng.* 315 (2017) 25–49.
- [8] M. He, D.F. Liang, B. Ren, J.Y. Li, S.D. Shao, Wave interactions with multi-float structures: SPH model, experimental validation, and parametric study, *Coastal Eng.* 184 (2023) 104333.
- [9] D. Molteni, A. Colagrossi, A simple procedure to improve the pressure evaluation in hydrodynamic context using the SPH, *Comput. Phys. Commun.* 180 (2009) 861–872.
- [10] J.J. Monaghan, R.A. Gingold, Shock simulation by the particle method SPH, *J. Comput. Phys.* 52 (1983) 374–389.
- [11] A. Colagrossi, M. Landrini, Numerical simulation of interfacial flows by smoothed particle hydrodynamics, *J. Comput. Phys.* 191 (2003) 448–475.
- [12] S. Marrone, M. Antuono, A. Colagrossi, G. Colicchio, D. Le Touzé, G. Graziani, 8-SPH model for simulating violent impact flows, *Comput. Methods Appl. Mech. Eng.* 200 (2011) 1526–1542.
- [13] J.J. Monaghan, SPH and Riemann Solvers, *J. Comput. Phys.* 136 (1997) 298–307.
- [14] A.N. Parshikov, Application of a solution to the Riemann problem in the SPH method, *Zhurnal Vychislitel'noi Matematiki i Matematicheskoi Fiziki (Computational Mathematics and Mathematical Physics)* 39 (1999) 1216–1225.
- [15] M. Antuono, A. Colagrossi, S. Marrone, D. Molteni, Free-surface flows solved by means of SPH schemes with numerical diffusive terms, *Comput. Phys. Commun.* 181 (2010) 532–549.
- [16] C. Zhang, X.Y. Hu, N.A. Adams, A weakly compressible SPH method based on a low-dissipation Riemann solver, *J. Comput. Phys.* 335 (2017) 605–620.
- [17] F.V. Sirokin, J.J. Yoh, A smoothed particle hydrodynamics method with approximate Riemann solvers for simulation of strong explosions, *Comput. Fluids*, 88 (2013) 418–429.
- [18] J.J. Monaghan, H. Pongracic, Artificial viscosity for particle methods, *Appl. Numer. Math.* 1 (1985) 187–194.
- [19] S. Inutsuka, Reformulation of smoothed particle hydrodynamics with Riemann solver, *J. Comput. Phys.* 179 (2002) 238–267.
- [20] P.N. Sun, C. Pilloton, M. Antuono, A. Colagrossi, Inclusion of an acoustic damper term in weakly-compressible SPH models, *J. Comput. Phys.* 483 (2023) 112056.
- [21] A. Khayyer, Y. Shimizu, T. Gotoh, H. Gotoh, Enhanced resolution of the continuity equation in explicit weakly compressible SPH simulations of incompressible free-surface fluid flows, *Appl. Math. Model.* 116 (2023) 84–121.
- [22] A. Dedner, F. Kemm, D. Kröner, C.D. Munz, T. Schnitzer, M. Wesenberg, Hyperbolic divergence cleaning for the MHD equations, *J. Comput. Phys.* 175 (2002) 645–673.
- [23] T.S. Tricco, D.J. Price, Constrained hyperbolic divergence cleaning for smoothed particle magnetohydrodynamics, *J. Comput. Phys.* 231 (2012) 7214–7236.
- [24] T.S. Tricco, D.J. Price, M.R. Bate, Constrained hyperbolic divergence cleaning in smoothed particle magnetohydrodynamics with variable cleaning speeds, *J. Comput. Phys.* 322 (2016) 326–344.
- [25] G. Fournakis, B.D. Rogers, R. Vacondio, An investigation on the divergence cleaning in weakly compressible SPH, in: Proceedings of the 17th International SPHERIC Workshop, Rhodes Island, Greece, Published by The University of Manchester, UK, 2023, pp. 55–62. ISBN 978-1-3999-5885-1.
- [26] J.P. Morris, J.J. Monaghan, A switch to reduce SPH viscosity, *J. Comput. Phys.* 136 (1997) 41–50.
- [27] J.I. Read, T. Hayfield, SPHS: smoothed particle hydrodynamics with a higher order dissipation switch: SPH with a higher order dissipation switch, *Mon. Not. R. Astron. Soc.* 422 (2012) 3037–3055.
- [28] P.W. Randles, L.D. Libersky, Smoothed particle hydrodynamics: some recent improvements and applications, *Comput. Methods Appl. Mech. Eng.* 139 (1996) 375–408.
- [29] V. Zago, L.J. Schulze, G. Bilotta, N. Almashan, R.A. Dalrymple, Overcoming excessive numerical dissipation in SPH modeling of water waves, *Coastal Eng.* 170 (2021) 104018.
- [30] H.G. Lyu, P.N. Sun, P.Z. Liu, X.T. Huang, A. Colagrossi, Derivation of an improved smoothed particle hydrodynamics model for establishing a three-dimensional numerical wave tank overcoming excessive numerical dissipation, *Phys. Fluids* 35 (2023) 67102.
- [31] P.P. Wang, Z.F. Meng, A.M. Zhang, F.R. Ming, P.N. Sun, Improved particle shifting technology and optimized free-surface detection method for free-surface flows in smoothed particle hydrodynamics, *Comput. Methods Appl. Mech. Eng.* 357 (2019) 112580.
- [32] D. Avesani, M. Dumbser, A. Bellin, A new class of Moving-Least-Squares WENO-SPH schemes, *J. Comput. Phys.* 270 (2014) 278–299.
- [33] C. Zhang, G.M. Xiang, B. Wang, X.Y. Hu, N.A. Adams, A weakly compressible SPH method with WENO reconstruction, *J. Comput. Phys.* 392 (2019) 1–18.
- [34] R. Antonia, R. Vacondio, D. Avesani, M. Righetti, M. Renzi, A WENO SPH scheme with improved transport velocity and consistent divergence operator, *Comput. Part. Mech.* (2023) 1–20.
- [35] B. Xue, S.P. Wang, Y.X. Peng, A.M. Zhang, A novel coupled Riemann SPH-RKPM model for the simulation of weakly compressible fluid–structure interaction problems, *Ocean Eng.* 266 (2022) 112447.
- [36] A. Khayyer, H. Gotoh, Y. Shimizu, T. Gotoh, An improved Riemann SPH-Hamiltonian SPH coupled solver for hydroelastic fluid-structure interactions, *Eng. Anal. Bound. Elem.* 158 (2024) 332–355.
- [37] A. Khayyer, H. Gotoh, Y. Shimizu, Comparative study on accuracy and conservation properties of two particle regularization schemes and proposal of an optimized particle shifting scheme in ISPH context, *J. Comput. Phys.* 332 (2017) 236–256.
- [38] P.N. Sun, A. Colagrossi, S. Marrone, M. Antuono, A.M. Zhang, Multi-resolution Delta-plus-SPH with tensile instability control: towards high Reynolds number flows, *Comput. Phys. Commun.* 224 (2018) 63–80.
- [39] G.K. Batchelor, A.D. Young, An introduction to fluid mechanics, *J. Appl. Mech.* 35 (1968) 624.
- [40] A.J.C. Crespo, J.M. Domínguez, B.D. Rogers, M. Gómez-Gesteira, S. Longshaw, R. Canelas, R. Vacondio, A. Barreiro, O. García-Feal, DualSPHysics: open-source parallel CFD solver based on smoothed particle hydrodynamics (SPH), *Comput. Phys. Commun.* 187 (2015) 204–216.
- [41] H. Gotoh, T. Shibahara, T. Sakai, Sub-particle-scale turbulence model for the MPS method - Lagrangian flow model for hydraulic engineering, *Comput. Fluid Dyn. J.* 9 (2001) 339–347.
- [42] H. Wendland, Piecewise polynomial, positive definite and compactly supported radial functions of minimal degree, *Adv. Comput. Math.* 4 (1995) 389–396.
- [43] G. Fournakis, J.M. Domínguez, R. Vacondio, B.D. Rogers, Local uniform stencil (LUST) boundary condition for arbitrary 3-D boundaries in parallel smoothed particle hydrodynamics (SPH) models, *Comput. Fluids*, 190 (2019) 346–361.
- [44] J.J. Monaghan, A. Rafiee, A simple SPH algorithm for multi-fluid flow with high density ratios, *Int. J. Numer. Methods Fluids*, 71 (2013) 537–561.
- [45] J.J. Monaghan, A. Kos, Solitary waves on a Cretan beach, *J. Waterway Port Coastal Ocean Eng.* 125 (1999) 145–155.
- [46] S. Adami, X.Y. Hu, N.A. Adams, A generalized wall boundary condition for smoothed particle hydrodynamics, *J. Comput. Phys.* 231 (2012) 7057–7075.
- [47] P.N. Sun, A. Colagrossi, S. Marrone, M. Antuono, A.M. Zhang, A consistent approach to particle shifting in the 8-Plus-SPH model, *Comput. Methods Appl. Mech. Eng.* 348 (2019) 912–934.
- [48] H.G. Lyu, P.N. Sun, Further enhancement of the particle shifting technique: towards better volume conservation and particle distribution in SPH simulations of violent free-surface flows, *Appl. Math. Model.* 101 (2022) 214–238.
- [49] R.M. Nestor, M. Basa, M. Lastiwka, N.J. Quinlan, Extension of the finite volume particle method to viscous flow, *J. Comput. Phys.* 228 (2009) 1733–1749.
- [50] R. Xu, P. Stansby, D. Laurence, Accuracy and stability in incompressible SPH (ISPH) based on the projection method and a new approach, *J. Comput. Phys.* 228 (2009) 6703–6725.
- [51] S.J. Lind, R. Xu, P.K. Stansby, B.D. Rogers, Incompressible smoothed particle hydrodynamics for free-surface flows: a generalised diffusion-based algorithm for stability and validations for impulsive flows and propagating waves, *J. Comput. Phys.* 231 (2012) 1499–1523.
- [52] S. Marrone, A. Colagrossi, D. Le Touzé, G. Graziani, Fast free-surface detection and level-set function definition in SPH solvers, *J. Comput. Phys.* 229 (2010) 3652–3663.
- [53] J. Michel, A. Vergnaud, G. Oger, C. Hermange, D. Le Touzé, On Particle Shifting Techniques (PSTs): analysis of existing laws and proposition of a convergent and multi-invariant law, *J. Comput. Phys.* 459 (2022) 110999.
- [54] P. Rastelli, R. Vacondio, J.C. Marongiu, An arbitrarily Lagrangian–Eulerian SPH scheme with implicit iterative particle shifting procedure, *Comput. Methods Appl. Mech. Eng.* 414 (2023) 116159.
- [55] S. Marrone, A. Colagrossi, A. Di Mascio, D. Le Touzé, Prediction of energy losses in water impacts using incompressible and weakly compressible models, *J. Fluids Struct.* 54 (2015) 802–822.
- [56] C. Pilloton, P.N. Sun, X. Zhang, A. Colagrossi, Volume conservation issue within SPH models for long-time simulations of violent free-surface flows, *Comput. Methods Appl. Mech. Eng.* 419 (2024) 116640.
- [57] P.P. Wang, A.M. Zhang, Z.F. Meng, F.R. Ming, X.L. Fang, A new type of WENO scheme in SPH for compressible flows with discontinuities, *Comput. Methods Appl. Mech. Eng.* 381 (2021) 113770.
- [58] Z.F. Meng, P.P. Wang, A.M. Zhang, F.R. Ming, P.N. Sun, A multiphase SPH model based on Roe's approximate Riemann solver for hydraulic flows with complex interface, *Comput. Methods Appl. Mech. Eng.* 365 (2020) 112999.
- [59] A. Khayyer, Y. Shimizu, C.H. Lee, A. Gil, H. Gotoh, J. Bonet, An improved updated Lagrangian SPH method for structural modelling, *Comput. Part. Mech.* (2023) 1–32.
- [60] M. Rezavand, C. Zhang, X. Hu, Generalized and efficient wall boundary condition treatment in GPU-accelerated smoothed particle hydrodynamics, *Comput. Phys. Commun.* 281 (2022) 108507.
- [61] Z.F. Meng, P.N. Sun, Y. Xu, P.P. Wang, A.M. Zhang, High-order Eulerian SPH scheme through W/TENO reconstruction based on primitive variables for simulating incompressible flows, *Comput. Methods Appl. Mech. Eng.* 427 (2024) 117065.
- [62] D. Le Touzé, A. Colagrossi, G. Colicchio, M. Greco, A critical investigation of smoothed particle hydrodynamics applied to problems with free-surfaces, *Int. J. Numer. Methods Fluids.* 73 (2013) 660–691.
- [63] M. Antuono, S. Marrone, A. Colagrossi, B. Bouscasse, Energy balance in the 8-SPH scheme, *Comput. Methods Appl. Mech. Eng.* 289 (2015) 209–226.
- [64] L. Lobovský, E. Botia-Vera, F. Castellana, J. Mas-Soler, A. Souto-Iglesias, Experimental investigation of dynamic pressure loads during dam break, *J. Fluids Struct.* 48 (2014) 407–434.
- [65] A. Souto-Iglesias, G. Bulian, E. Botia-Vera, A set of canonical problems in sloshing. Part 2: influence of tank width on impact pressure statistics in regular forced angular motion, *Ocean Eng.* 105 (2015) 136–159.

- [66] K.M.T. Kleefsman, G. Fekken, A.E.P. Veldman, B. Iwanowski, B. Buchner, A volume-of-fluid based simulation method for wave impact problems, *J. Comput. Phys.* 206 (2005) 363–393.
- [67] G. Oger, S. Marrone, D.Le Touzé, M. de Leffe, SPH accuracy improvement through the combination of a quasi-Lagrangian shifting transport velocity and consistent ALE formalisms, *J. Comput. Phys.* 313 (2016) 76–98.
- [68] A. Colagrossi, A Meshless Lagrangian Method for Free-Surface and Interface Flows with Fragmentation, Thesis, University of Rome, La Sapienza, 2005.
- [69] S. Marrone, A. Colagrossi, M. Antuono, C. Lugni, M.P. Tulin, A 2D+ t SPH model to study the breaking wave pattern generated by fast ships, *J. Fluids. Struct.* 27 (2011) 1199–1215.
- [70] Z.T. Ye, X.Z. Zhao, Investigation of water-water interface in dam break flow with a wet bed, *J. Hydrol.* 548 (2017) 104–120.
- [71] P.N. Sun, F.R. Ming, A.M. Zhang, Numerical simulation of interactions between free surface and rigid body using a robust SPH method, *Ocean Eng.* 98 (2015) 32–49.
- [72] X.F. Yang, M.B. Liu, S.L. Peng, C.G. Huang, Numerical modeling of dam-break flow impacting on flexible structures using an improved SPH-EBG method, *Coastal Eng.* 108 (2016) 56–64.
- [73] A. English, J.M. Domínguez, R. Vacondio, A.J.C. Crespo, P.K. Stansby, S.J. Lind, L. Chiapponi, M. Gómez-Gesteira, Modified dynamic boundary conditions (mDBC) for general-purpose smoothed particle hydrodynamics (SPH): application to tank sloshing, dam break and fish pass problems, *Comput. Part. Mech.* 9 (2022) 1–15.
- [74] Y.L. Zhang, D.C. Wan, MPS-FEM coupled method for sloshing flows in an elastic tank, *Ocean Eng.* 152 (2018) 416–427.
- [75] D. Winkler, M. Meister, M. Rezavand, W. Rauch, gpuSPHASE—A shared memory caching implementation for 2D SPH using CUDA, *Comput. Phys. Commun.* 213 (2017) 165–180.
- [76] L. Chiron, M. de Leffe, G. Oger, D.Le Touzé, Fast and accurate SPH modelling of 3D complex wall boundaries in viscous and non viscous flows, *Comput. Phys. Commun.* 234 (2019) 93–111.
- [77] I. Martínez-Estevez, J.M. Domínguez, B. Tagliafierro, R.B. Canelas, O. García-Feal, A.J.C. Crespo, M. Gómez-Gesteira, Coupling of an SPH-based solver with a multiphysics library, *Comput. Phys. Commun.* 283 (2023) 108581.
- [78] A. Mokos, B.D. Rogers, P.K. Stansby, J.M. Domínguez, Multi-phase SPH modelling of violent hydrodynamics on GPUs, *Comput. Phys. Commun.* 196 (2015) 304–316.